行政院國家科學委員會專題研究計劃成果報告。
交通部　氣象局

◎◎◎◎◎◎◎◎◎◎◎◎◎◎◎◎◎◎◎◎◎◎◎◎◎◎◎◎◎◎
◎　　　　　　　　　　　　　　　　　　　　　　　　◎
◎　台灣地區降水之短期預報的研究　（Ⅱ）　　　　◎
◎　　　　　　　　　　　　　　　　　　　　　　　　◎
◎◎◎◎◎◎◎◎◎◎◎◎◎◎◎◎◎◎◎◎◎◎◎◎◎◎◎◎◎◎

計劃編號：　NSC 83-0618-M-008-001
　　　　　　NSC 83-0202-M-008-005
　　　　　　CWB83-2M-13-3

執行期間：

計劃主持人：張隆男

共同主持人：陳景森

協同主持人：林沛練　陳台琦

處理方式：　☑可立即對外提供參考。
（請打勾）　口一年後可對外提供參考。
　　　　　　口兩年後可對外提供參考。
　　　　　　（必要時，本會得延展發表時限）

執行單位：國立中央大學

中華民國 83 年 10 月 10 日

摘要

　　台灣位於亞熱帶，四面環海，境內地行複雜，氣流受到地形的影響，會產生分流、加速或漩渦，影響降水系統的平移或發展，而地形提供冷熱源，使得降水的發生、增强及減弱，常常在短時間內有很大的變化。當降水在某一地區，短時間內急速增加，長可能帶來豪雨，爲了掌握這些變化，並提出對劇烈降水的預警，降水短期預報的研究不可缺乏。如何做好即時，則有賴資料的收集是否充裕，降水的性質是否能事先了解。根據Doswell（1986），McGinley（1986）的研究，欲做好短期預報，下列氣象資料必需得到：

a. 傳統天氣資料。

b. 台灣地區連續地面氣象資料。

c. 傳統及都普勒雷達資料。

d. 連續高空風資料。

e. 高時間解析度的低對流層風及溫度資料（整合性探空系統資料）。

f. 包括台灣地形 $meso-\beta$ 及 $meso-\gamma$ 尺度的模式模擬資料。

　　在第二年的計劃，我們將注重現有儀器的整合，資料的匯整，雷達資料處理顯示用圖形工作站及觀測資料整合分析工作站的建制，模式模擬個案的初步探討找出降水機制。我們希望透過氣象資料的研判及個案數值模擬，對於做好台灣地區降水的短期預報有個好的準則。

1

Abstract

Taiwan island is located in the subtropicacl area. High mountain region orientated from north to south. The splitting of airflow, the acceleration of wind speed and lee-vortex will influence the advection of precipitation system. Besides that, since mountain acts as the sources and / or sink of heat and moisture, the occurrence, the duration , the intensifying and the decaying of the precipitations ccan vary in a very short time. To understanding and to make a good short - range forcasting of those phenomenon are very important for researchers. According to Doswell (1986) and McGinley (1986) the gathering of the meteorogical information as soon as possible is essential to the short - range forecaster . The following meteorogical data are needed:

a. Convectional meteorological data.

b. HIgh spacial and temporal resolution surface meteorological data in Taiwan area.

c. VHF wind data.

e. Integrated sounding system data.

f. $meso - \beta$ and $meso - \gamma$ model simulation data.

In the second year we will focus on the gathering meteorological data from existing system , the purching two " work stations " to analyze the radar data and convectional data , respectively , and analyze some preliminary simulation results. We hope through this " team - work " type study. We can find some good methods for short - range forecasting .

Key words : Short - range Forecasting

一、台灣地區降水之短期預報：

　　台灣位於亞熱帶，四面環海，境內地形複雜，氣流受到地形阻擋有很大的變化。如圖1，不同性值得氣流對降水系統的平移，有很大的影響。而且由氣流所產生的輻合、散場對降水系統平移，有很大的影響。而且由氣流所產生的輻合、散場對降水系統的產生及發生有很大的影響。而降水發生的地點，降水的增強及減弱常常在間內有很大的變化。在TAMEX期間，由於氣象資料較充足，我們可以看到降水的相當快速(圖6)，如在IOP 2，颮線與陣風鋒面相交後回波的變化(圖7)，在IOP 8，台灣山區產生的降水雲系(圖8)的變化亦顯快速，隔月後，鋒面通過本省降水的分布相當不均勻(圖9)。在IOP 13，鋒面南移，在台中地區豪雨的個案(圖10)，其中，回波的變化在台中地區相當劇烈，以上這些觀測現象，再再說明台灣地區降水的變化相當快速，因此，為了掌握這些變化，並對劇烈降水能夠提出預警，降水短期預報的研究不可缺乏。

　　根據Doswell(1986)的研究，欲做好短期預報研究，有幾個方法要注意(圖11)，這些方法如中尺度模式、大尺度模式、氣候值、線性外延法以及氣象人員物理模式。再根據McGinley(1986)的研究，作好即時預報的工具有傳統雷達、都普勒雷達、衛星、探空資料以及傳統天氣資料。國科會與中央大學合資所採購的ISS系統，於1992 - 1993在NAURU參加TOGA / COARE的研究，初步資料結果描述如下，圖12a是斜溫圖，一天最多可觀測12次，由圖12a可以迅速了解大氣的垂直結構，對於判別降水的特性有很大的幫助(Weismann and Klemp，1986)如此我們可以每隔兩小時得到降水的指標，對於短期降水的預報，必有很大的助益。圖12b及c是利用陣列天線發射電磁波來測量大氣水平風場的垂直分布情形。圖12b的解析度為98m，可測量到5km高。圖12c的解析度為238m，可測量到10km高，圖12b及c的測量時距為30 min，如果有必要，可提高到連續觀測，有了水平圖的詳細資料，對於降水系統的平移必能掌握。圖12d為1.5 km以下的濕位溫的時間變化圖，資料高度距為60m，時間間距為30 min，必要時可以連續觀測。有了這些資料，可以隨時了解低層穩定度的變化，對於降水系統的發生或延續可以有效掌握。另外ISS系統亦配備地面觀測儀器，一般地面的觀測要素皆可以得到。這些機器目前以搬回國科會貴儀器中心-中壢站，可接受各方的觀測使用要求。

　　降水預報中對於雨量的估計亦十分重要，雨量的估計可以用雷達回波與降水量的關係式來估計(Z-R關係式)。這種關係式與降水形態、季節、地點皆有很大的關係，在台灣地區對於用雷達回波來估計雨量的研究，以中央大學陳台琦教授作的最多，圖13a及b是她提供的，圖13a是利用中正雷達的降水回波與

氣象局北部自動雨量站資料所導出的 Z-R 關係式（1989 年 5 月 29 日）。圖 13b 是比較回波估計的雨量與地面觀測雨量的比較，在 24 小時降水量比較相關係數達 0.85，因此利用 Z-R 關係式，可以有效在海上或無雨量站的地方估計雨量，對於降水預報有莫大的助益。

氣流受到地形影響很大，利用模式來了解風場的變化是很重要的，$meso-\gamma$ 數值模式的發展有了初步成果（見附錄）。圖 14 是在 Froude number 為 0.2 下，模式中氣流通過理想山的情形，山前逆流，山後渦流的情形與 Smolarkiewicz and Rotunno（1989）類似。圖 15a 及 b 是 1987 年 6 月 20 日 1200 LST 及 1400 LST 的地面觀測資料，圖 16A 及 b 是 1987 年 6 月 20 日 1200 LST 及 1400 LST 的地面觀測資料，圖 16a 及 b 是利用模式模擬的結果，我們發現模式在外海地區（北部澎佳嶼，中部馬公及東南部蘭嶼）的風向與觀測資料符合，而在嘉南地區的風向，亦有不錯的結果。同時在台灣北部模擬風向為海風的形態，與觀測相當符合，因此模式的模擬風向，在目前可以當作預報的參考資料。這些模擬的結果是利用國科會補助的工作站完成的。而降水的因素，需要模式的繼續發展以及好的數值模擬工作站。若再能配合分析資料的新的工作站診斷分析各種可能收集到的資料，嘗試尋找可能影響降水的因素，以及第二、三年模式的修改，系統與必要周邊設備，而模式的發展也達到較好的地步後，我們才有能力作更進一步的個案研究，找出影響降水的重要因素。

降水短期預報的研究，最重要的部分包括即時收集資料之診斷分析以及降水演變特性之模擬，即時資料之研究包括各種綜觀傳統地面或探空之研究，降水回波雷達數據化資料衛星資料，VHF 雷達風場資料，邊界層鐵塔的風場資料以及整合性探空系統密集氣象要素的垂直分布資料的診斷分析。短期預報資料之分析具有資料量大，處理速度快的需求，另外對繪圖能力以及圖形識別顯示視覺化要求也有很高之要求，因此添購適當的工作站是很迫切的需要。因此本計劃已添購兩套工作站，一套是雷達資料處理顯示用圖形工作站，另一套是觀測資料整合分析工作站，利用這兩套工作站所具備的繪圖功能以及輸出輸入的特殊需求之特性，已確保整個研究及品質。
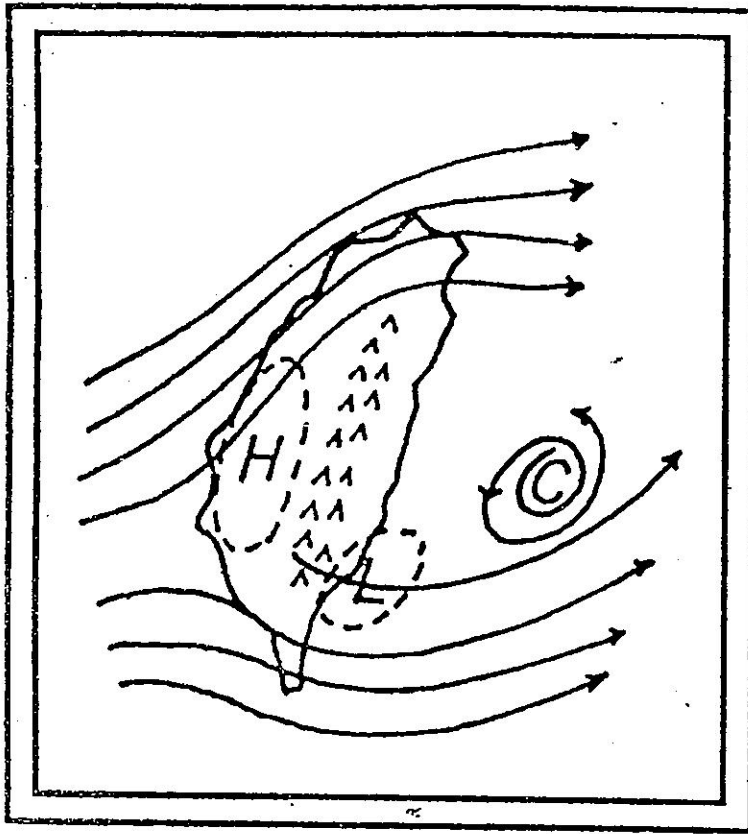
A conceptual model of the Taiwan southeast mesolow and mesocyclone. A stationary mesohigh forms on the upstream and a mesolow forms on the southeast of the CMR under a prevailing westerly or southwesterly flow. An additional moving mesocyclone develops to the east of the CMR if the impinging angle of the prevailing wind is large
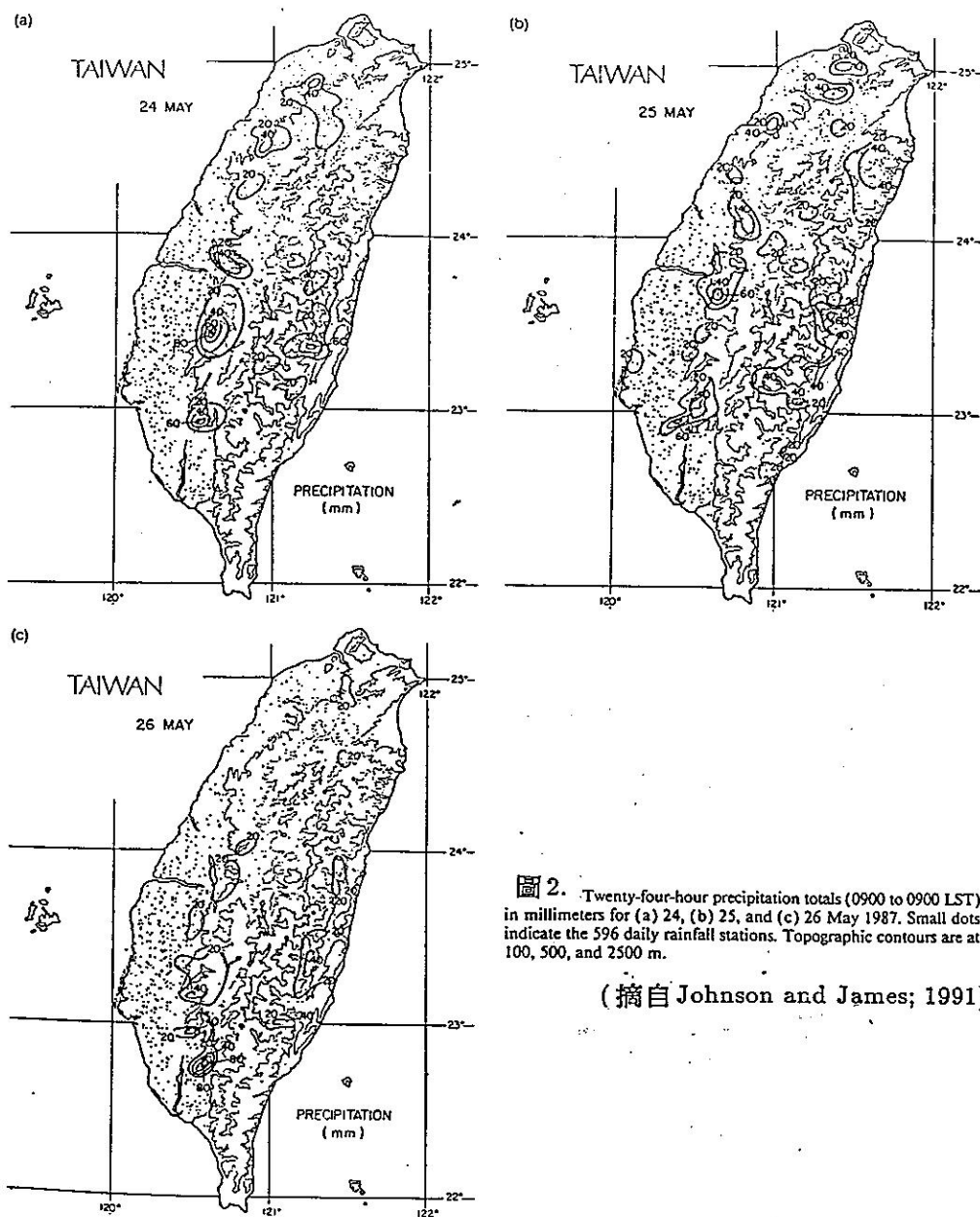
圖1. 摘自 LIN. et.al.(1992)

(a) TAIWAN 24 MAY PRECIPITATION (mm)

(b) TAIWAN 25 MAY PRECIPITATION (mm)

(c) TAIWAN 26 MAY PRECIPITATION (mm)

圖 2. Twenty-four-hour precipitation totals (0900 to 0900 LST) in millimeters for (a) 24, (b) 25, and (c) 26 May 1987. Small dots indicate the 596 daily rainfall stations. Topographic contours are at 100, 500, and 2500 m.

(摘自 Johnson and James; 1991)

convective in nature. The thunderstorms were most numerous on the 24th and 25th (Figs. 15a and 15b), diminishing considerably over the northern half of the island on the 26th (Fig. 15c) as drier air aloft moved over that region. A very interesting behavior of the convection on these 3 days was a preference for
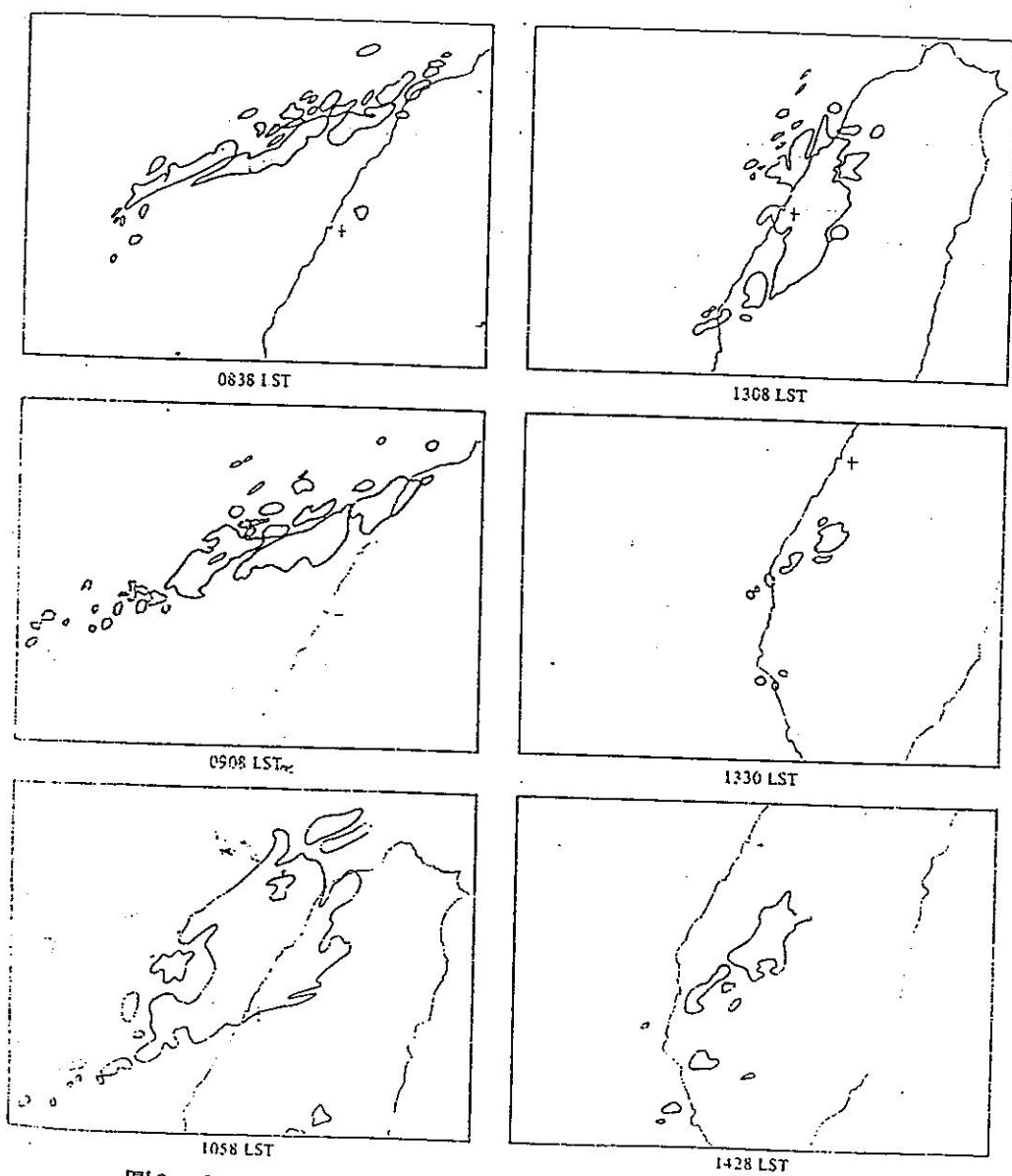
6

(a)

TAIWAN

24 MAY

PRECIPITATION
(mm)

(b)

TAIWAN

25 MAY

PRECIPITATION
(mm)

(c)

TAIWAN

26 MAY

PRECIPITATION
(mm)

圖 2. Twenty-four-hour precipitation totals (0900 to 0900 LST) in millimeters for (a) 24, (b) 25, and (c) 26 May 1987. Small dots indicate the 596 daily rainfall stations. Topographic contours are at 100, 500, and 2500 m.

(摘自 Johnson and James; 1991)

convective in nature. The thunderstorms were most numerous on the 24th and 25th (Figs. 15a and 15b), diminishing considerably over the northern half of the island on the 26th (Fig. 15c) as drier air aloft moved over that region. A very interesting behavior of the convection on these 3 days was a preference for

6

0838 LST

1308 LST

0908 LST

1330 LST

1058 LST

1428 LST

圖3. Detailed appearance of PPI echo system in the heavy rainfall period on Feb. 2, 1983.

摘自 Liao and Chen (1984)

1418

1758

1858

2008

1400

1700

2000
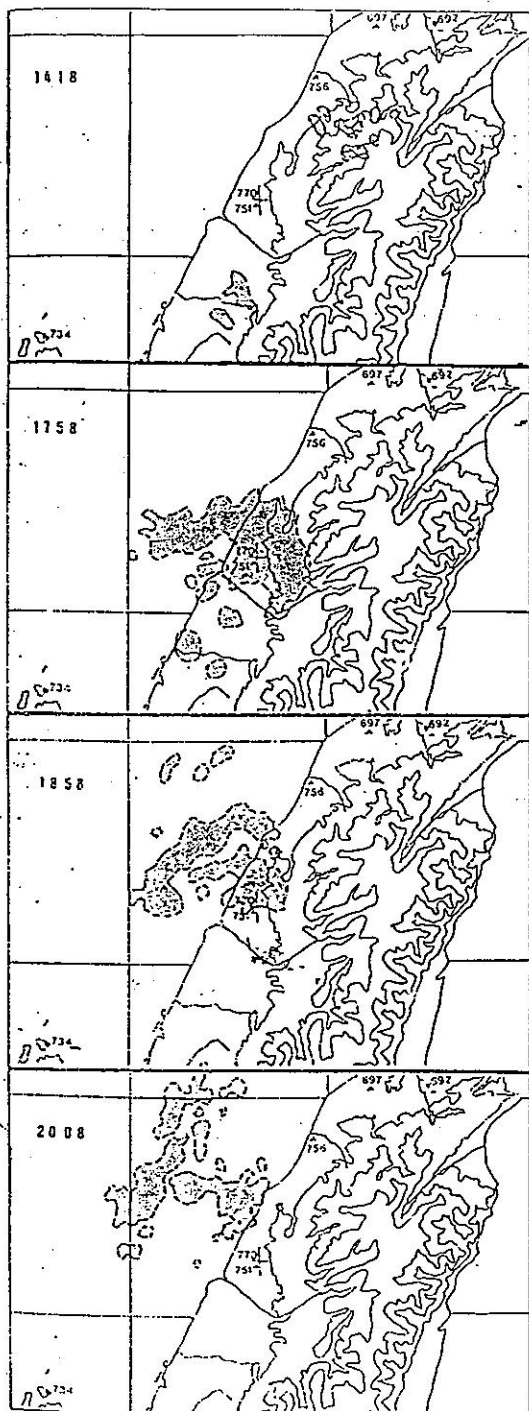
圖 4.

Selected PPI radar reflectivity factor pattern (shaded area) and satellite image (IR) showing convection area on July 17, 1985. The elevation angle of the radar was 0° except at 1418 (angle was 2°). The radar reflectivity factor was shown at 0 dB(Z) except at 1418 (3 dB(Z)).

摘自 Liao and Chen (1984)

8
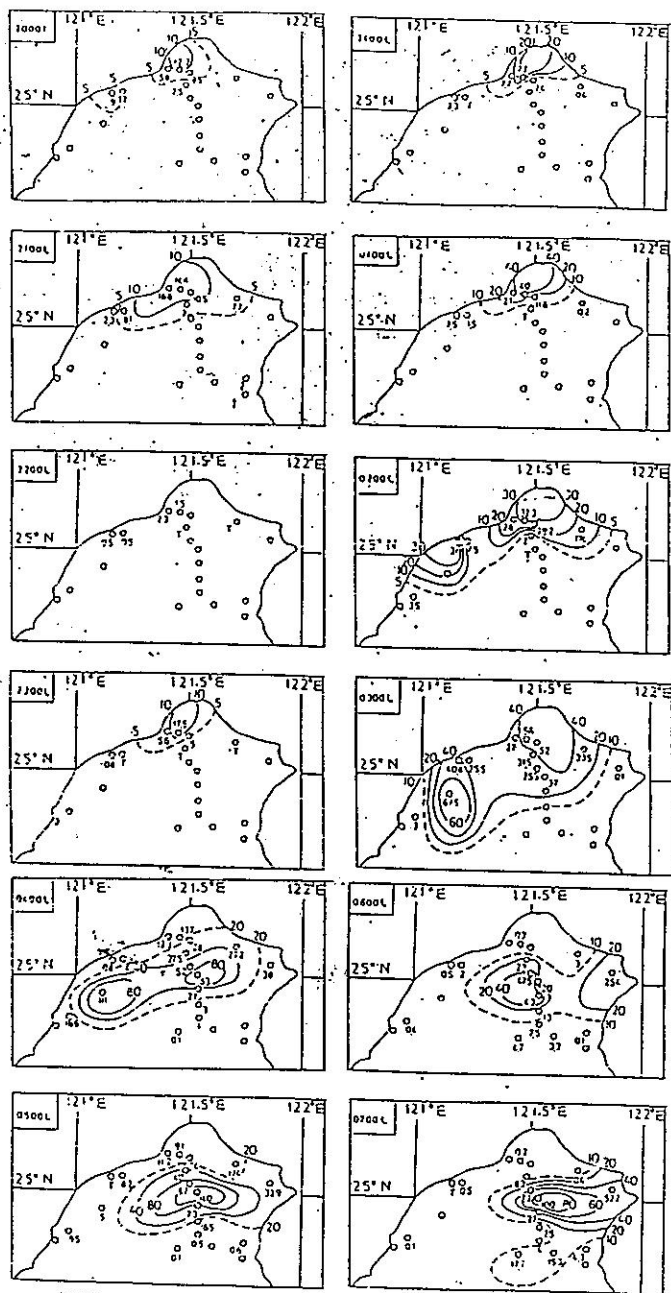
圖5. 1984年6月2～3日，台灣北部地區每小時降水量分布圖

單位：公釐

摘自丘台光與劉復誠(1985)
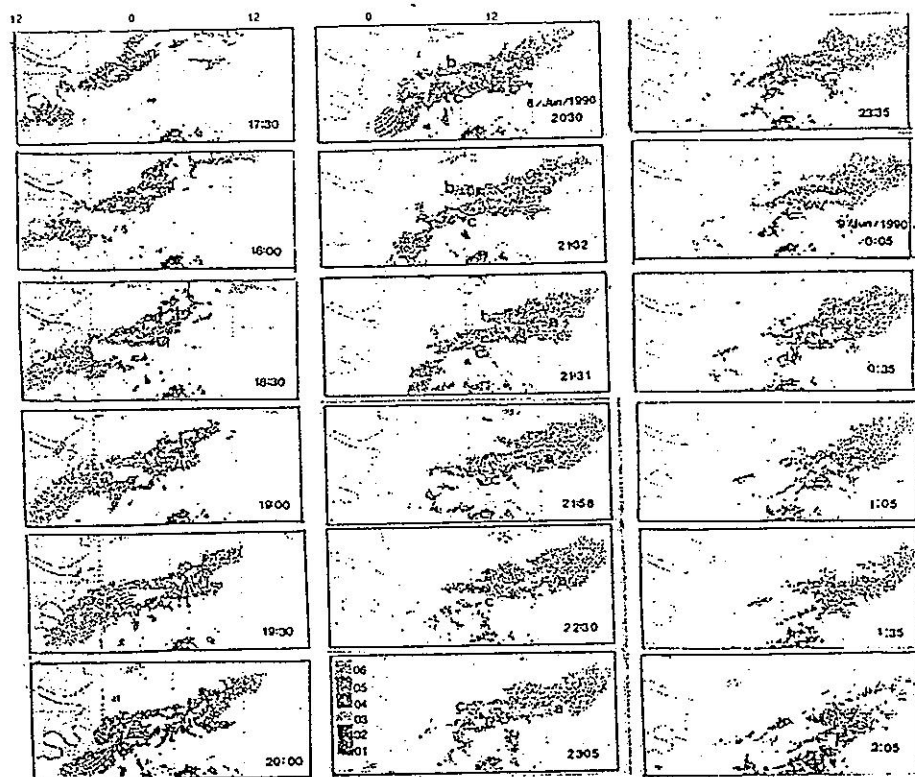
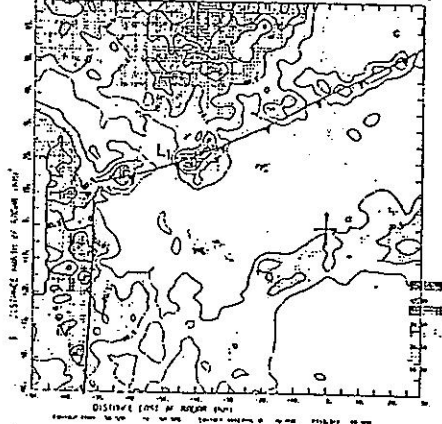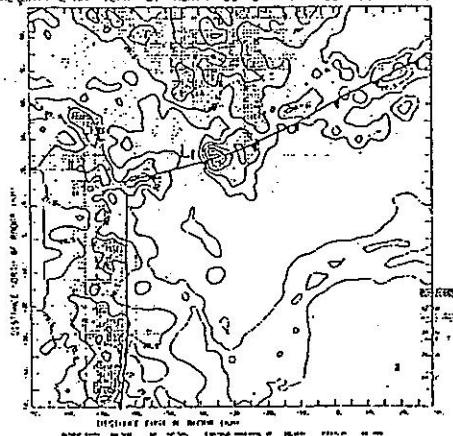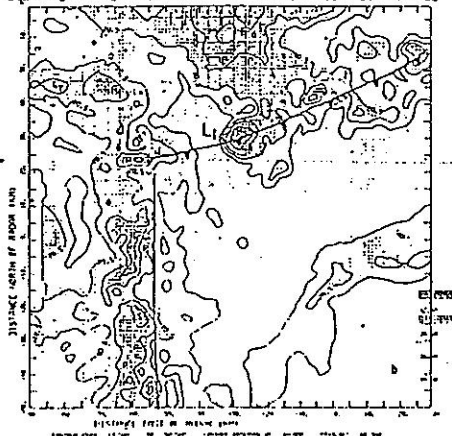圖6. 中大雷達每30分鐘PPI時間序列圖。

摘自王等(1991)
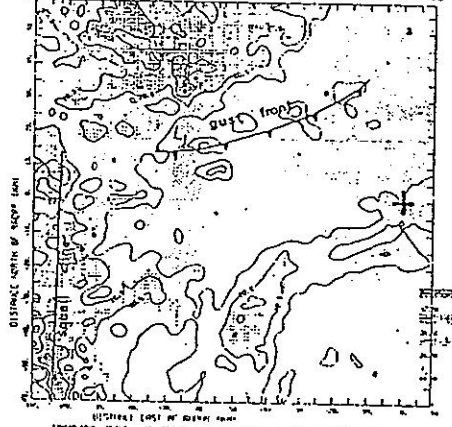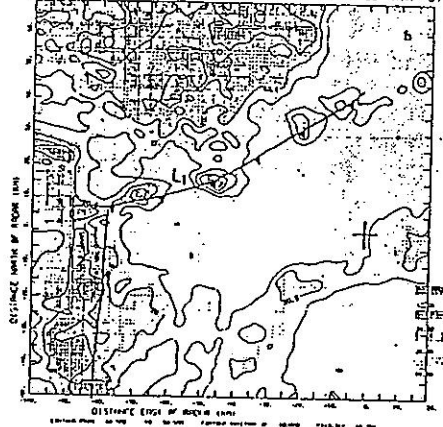
図7a. The reflectivity field at 2 km height at (a)
00:15, (b) 00:31, (c) 00:40 May 17, The
first contour was 10 dBZ, and the
contour interval was 10 dBZ. CAA radar
position is marked with a cross.

摘自 Wang (1989)

HEIGHT= 2 KM YEAR= 87 MONTH= 05 DAY= 17 HOUR= 00 MIN= 50

HEIGHT= 2 KM YEAR= 87 MONTH= 05 DAY= 17 HOUR= 01 MIN= 00

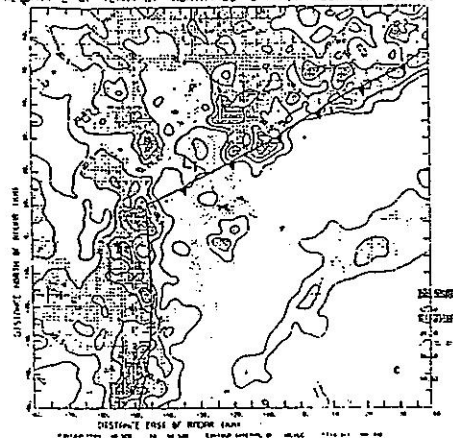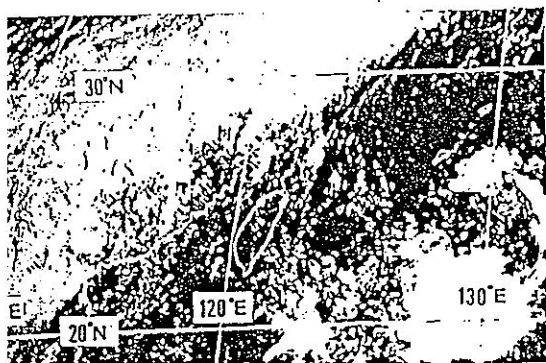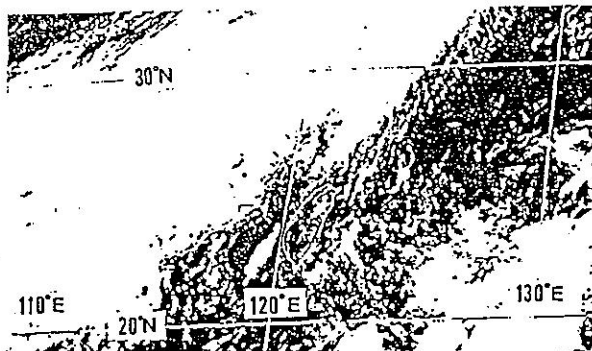HEIGHT= 2 KM YEAR= 87 MONTH= 05 DAY= 17 HOUR= 01 MIN= 10

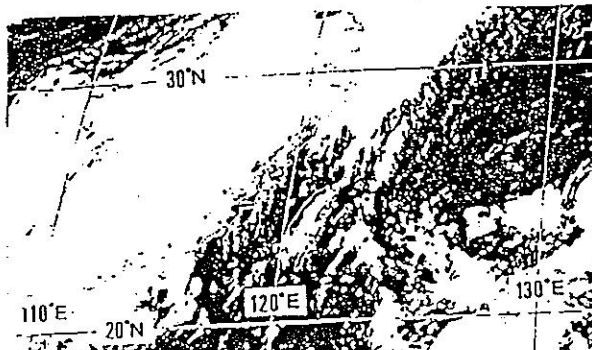圖 7b. Same as 圖 7a except for the reflectivity field at 2 km height at (a) 00:50, (b) 01:00, (c) 01:10 May 17.
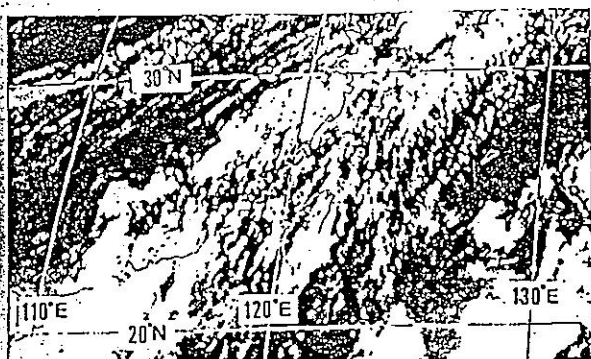
0800LST

1100LST

1300LST

圖8a. 1987年六月七日IR圖

1400LST

1700LST
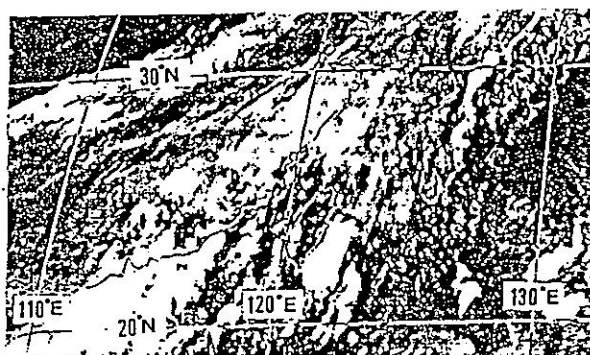
2000LST

2300LST

圖 8b. (續)

14
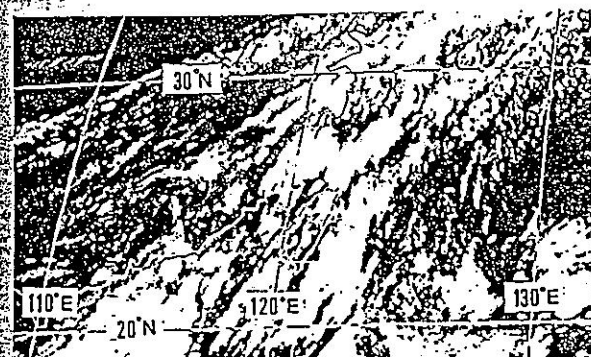
ACCUMULATED PRECIPITATION (mm) FOR
0000 LST 8 JUNE — 0000 LST 9 JUNE
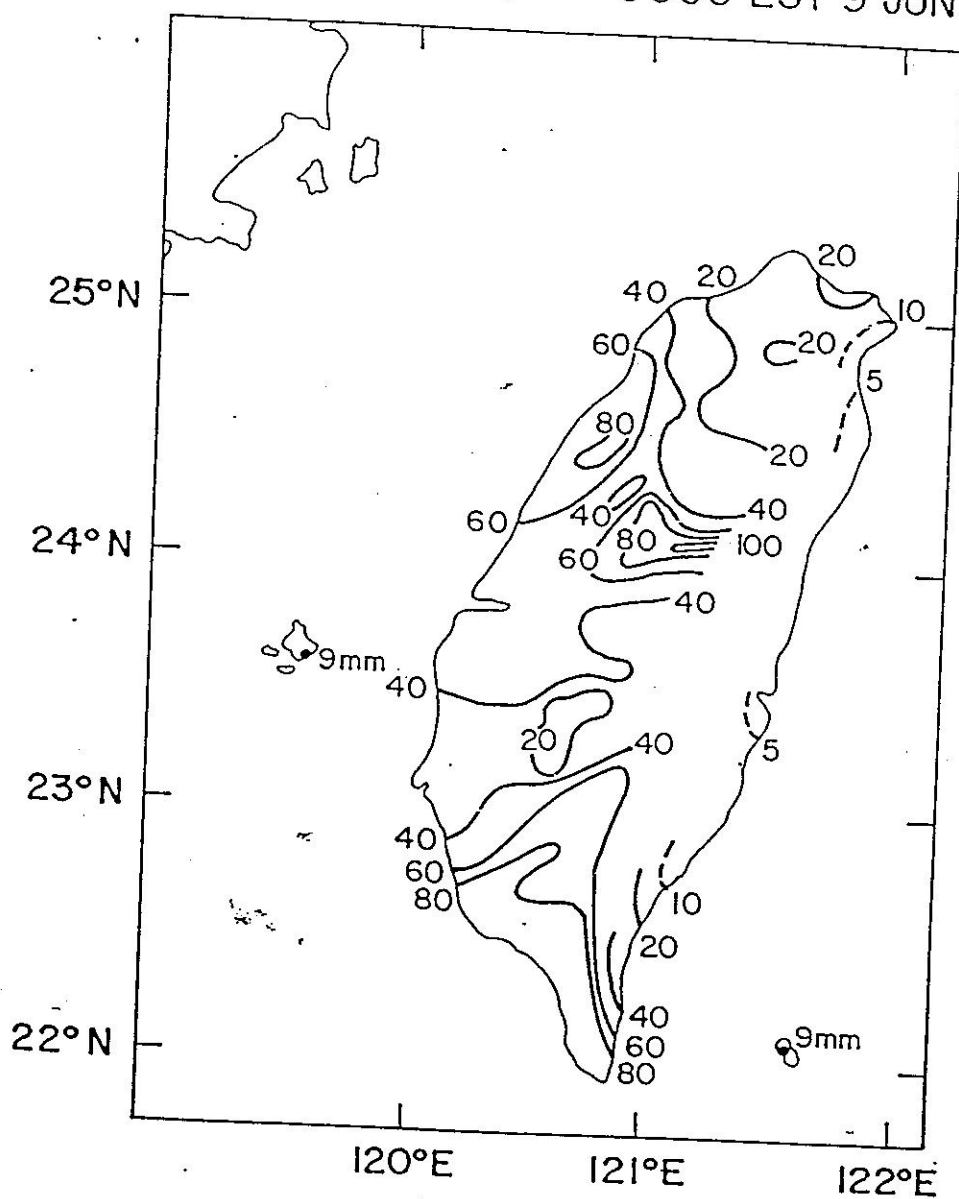
圖9.

（摘自 Trier. et.al; 1990）
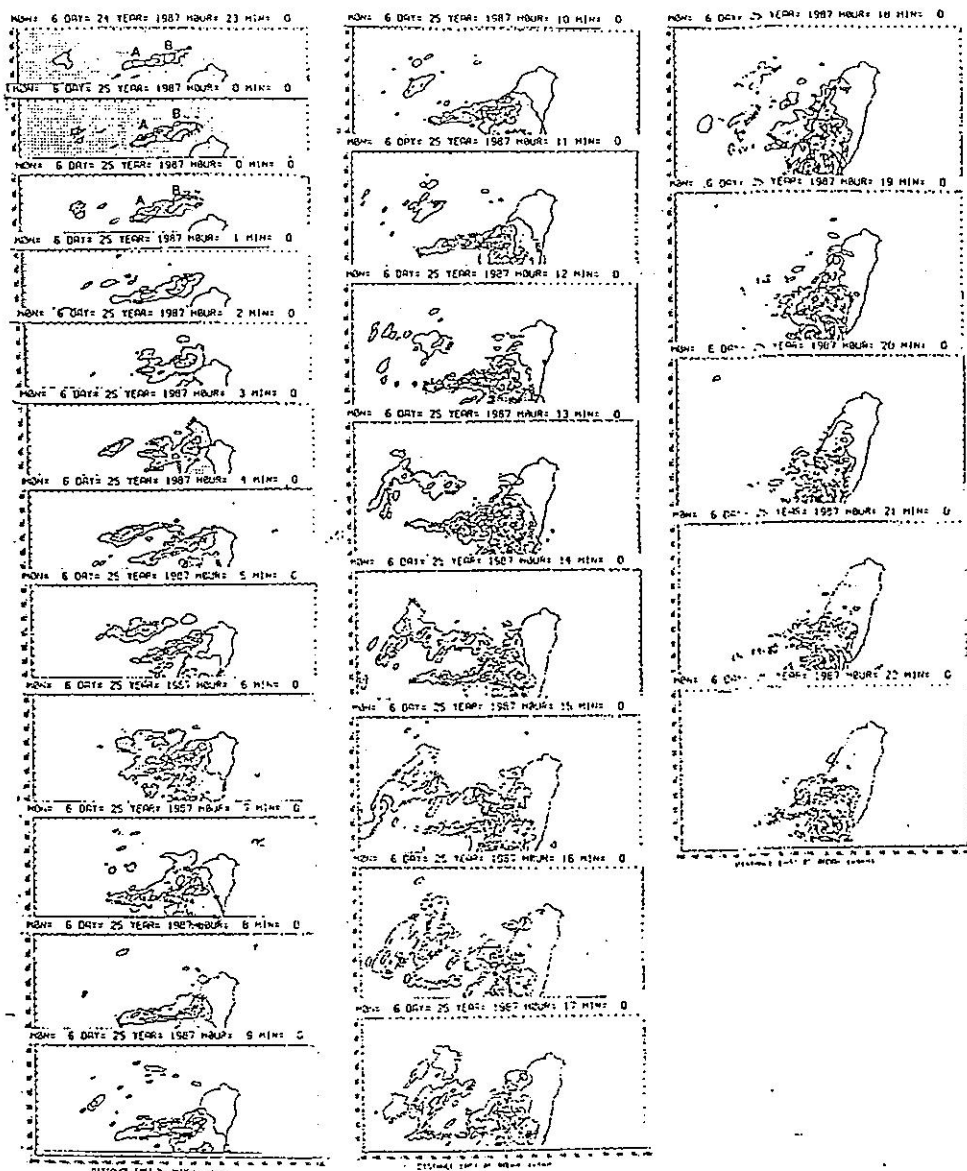
圖 10. The reflectivity field from Kaohsiung radar during 2300LST June 24 to 2200LST June 25, 1987. The first contour is 15.5 dBZ, the contour interval is 10 dBZ.

摘自 Lin et.al. (1989)

16
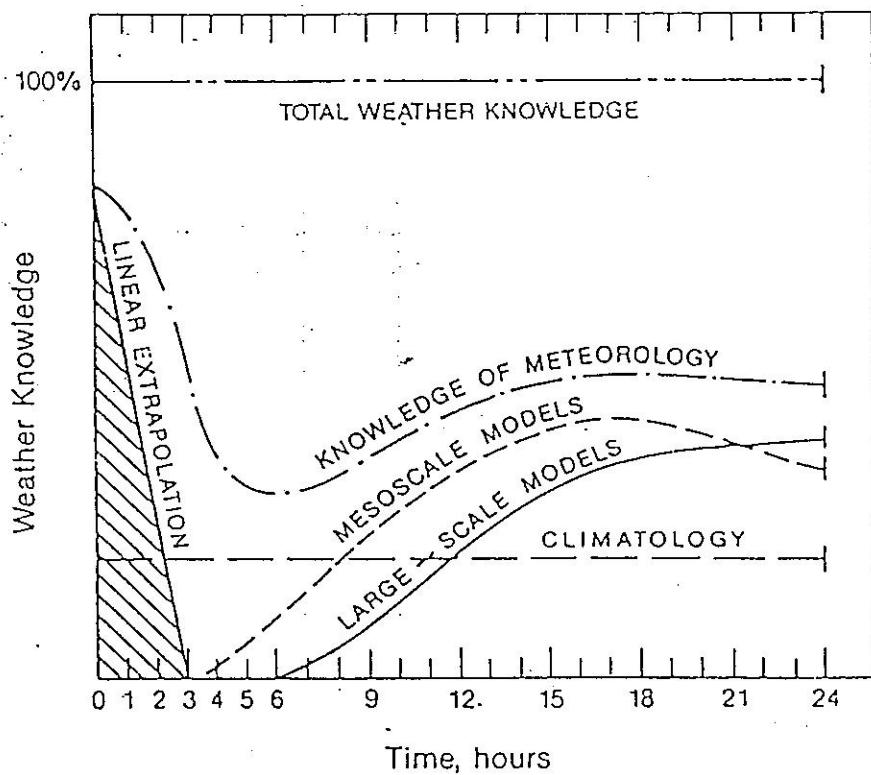
圖11. . . Effectiveness of different approaches to short-range (mesoscale) forecasting.

摘自 Doswell III (1986)

CLASS 10 SECOND DATA
TOGA/COARE: NAURU
GMT Launch Time (y,m,d,h,m,s):   1992, 10, 19, 10:47:03
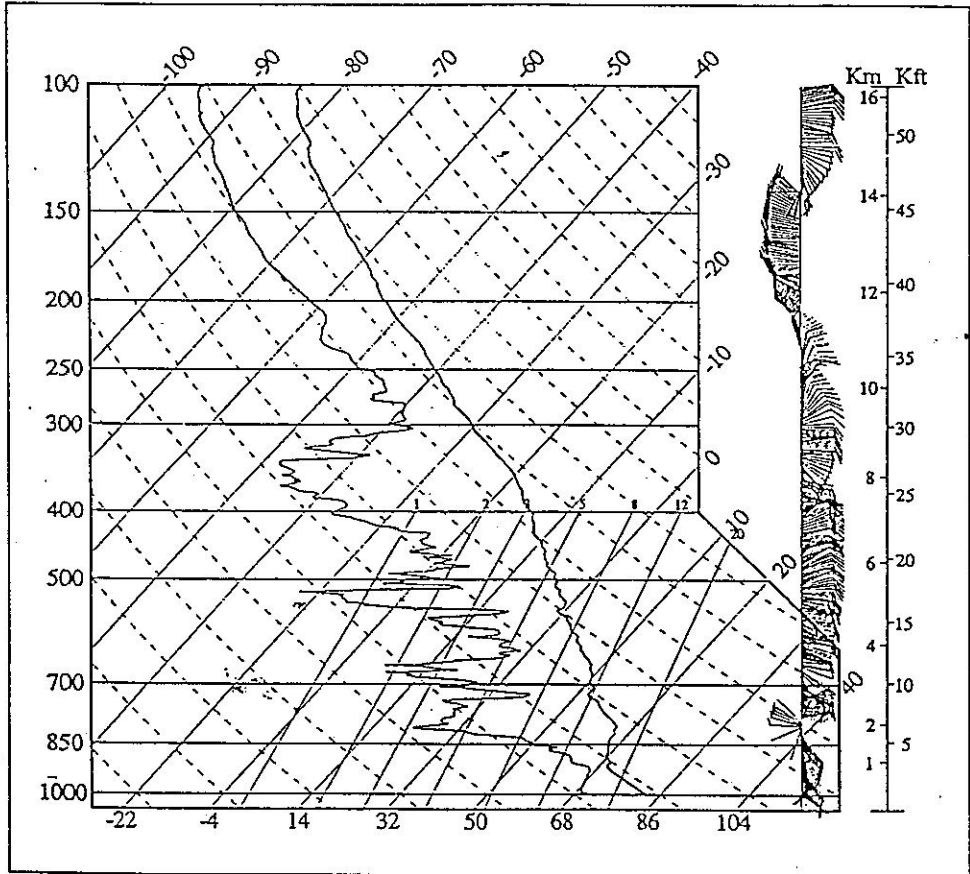
圖 12a：由ＣＬＡＳＳ系統資料所繪製成的斜溫圖

18

PROFILER WIND DATA
TOGA/COARE: NAURU
DATE: 1992, 10, 19
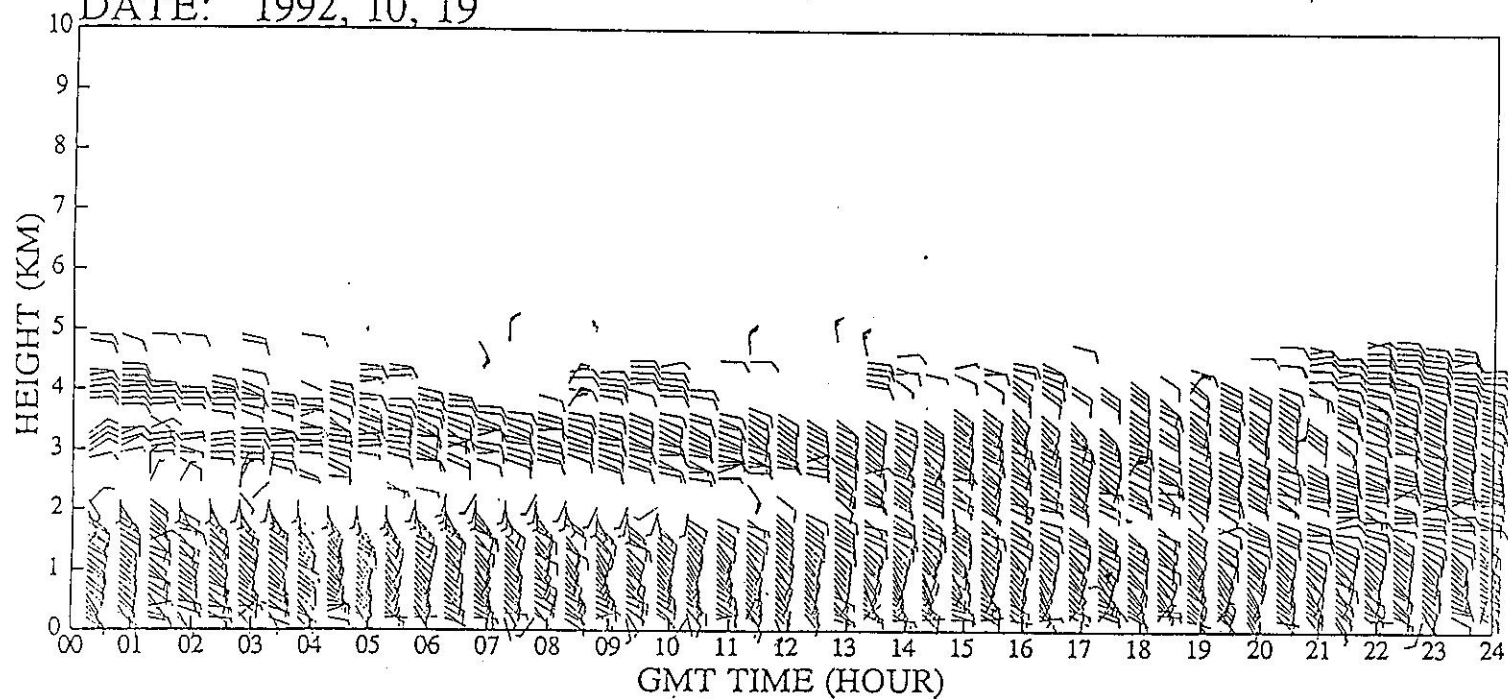
圖 12b：由ＰＲＯＦＩＬＥＲ系統高垂直解析度資
料所繪製成的風場變化圖
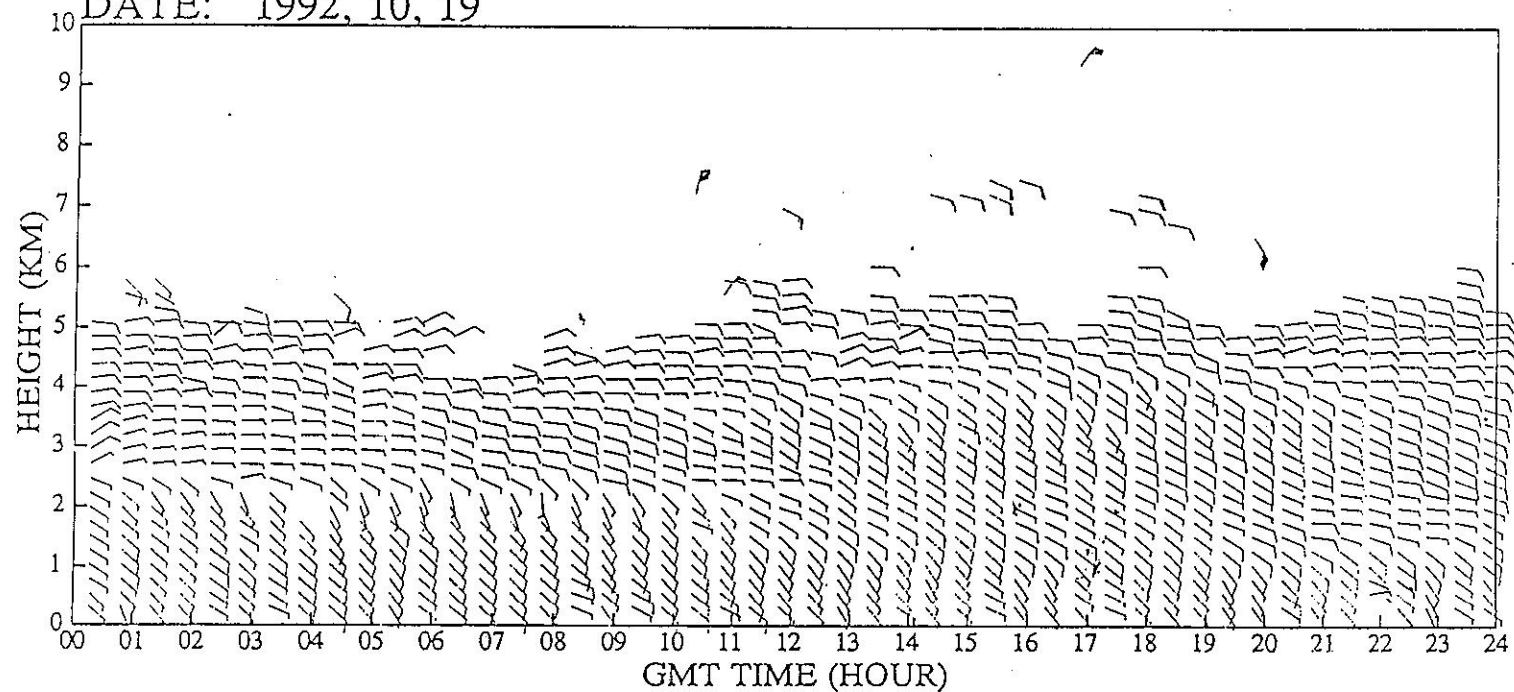
圖 12c.: 由ＰＲＯＦＩＬＥＲ系統低垂直解析度資
料所繪製成的風場變化圖

RASS TEMPERATURE DATA
TOGA/COARE: NAURU
DATE: 1992, 10, 19
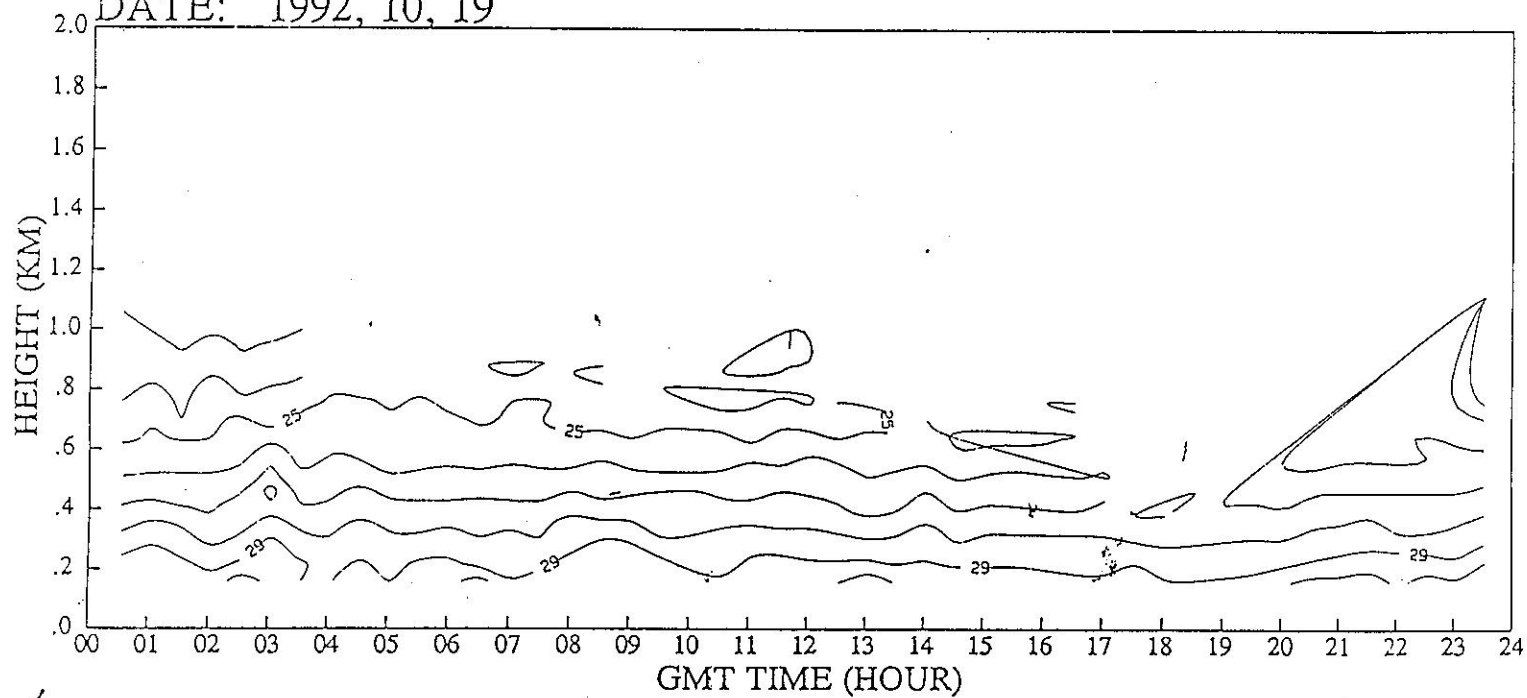
CONTOUR FROM 15 TO 30 CONTOUR INTERVAL OF 1

圖12d：由ＲＡＳＳ系統資料所繪製成的溫度變化圖
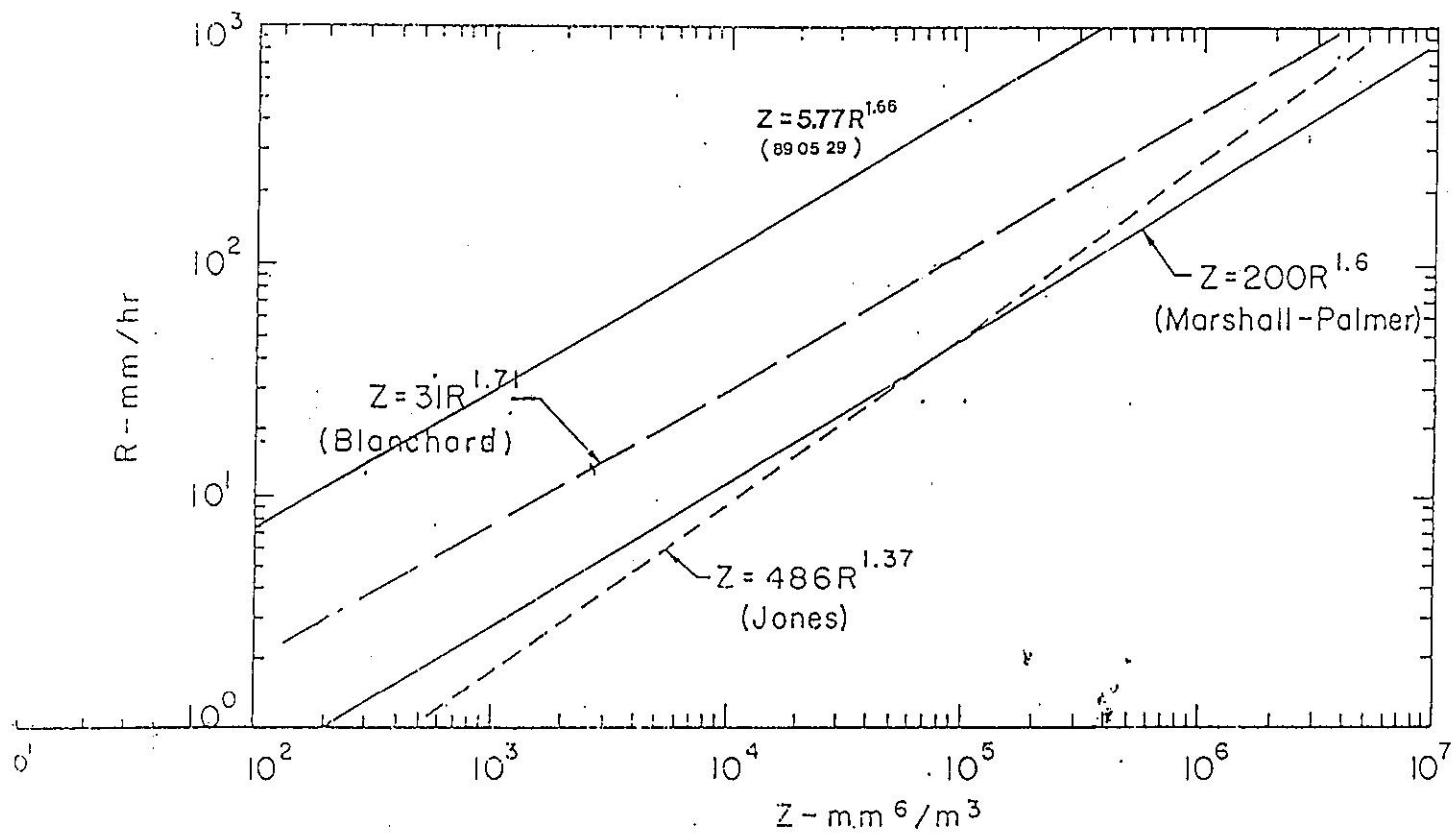
圖13a 中正雷達 1989.05.29. 之Z-R關係式和國外經驗式的比較.

TOTAL : 23 STOPS					
開始時間 : 5290543	5290943	5291443	5291943	5300043	5300543
測站累積雨量　　（mm）	56.4	79.6	111.0	113.8	118.6
回波估算累積雨量(mm)	43.6	75.5	114.2	118.3	121.8
兩者相關性	0.868	0.658	0.690	0.813	0.846

圖 13b

THE 1ST LAYER STREAMLINES
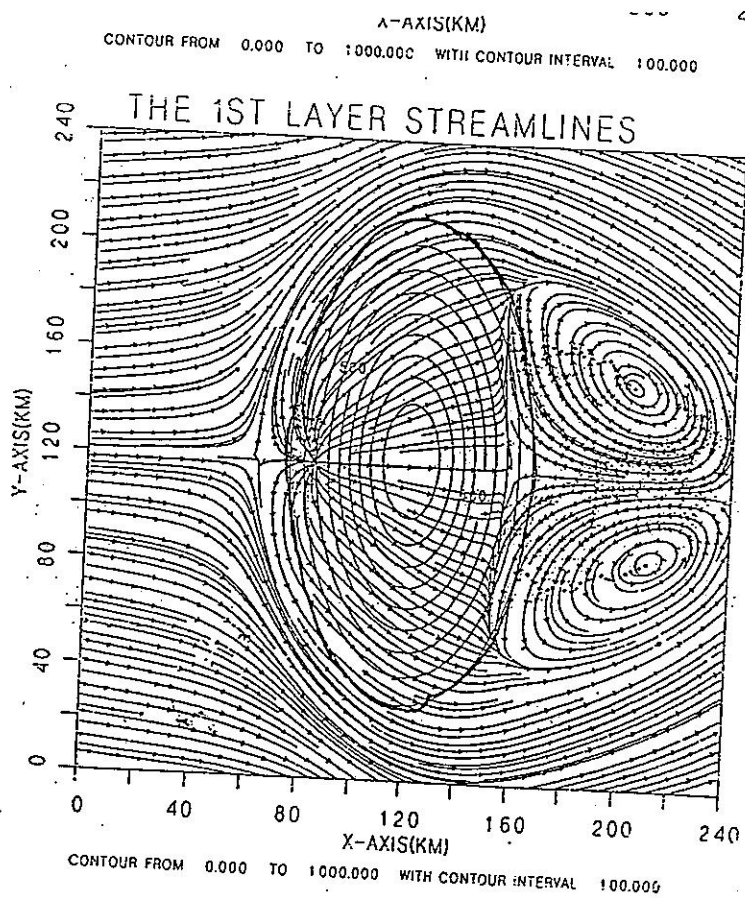
$$Fr = 0.2 = \frac{U}{NH}$$

$$\triangle x : 2km$$

$$\triangle y : 2km$$

圖14. Smolarkiewioz and Rotunno (1989)
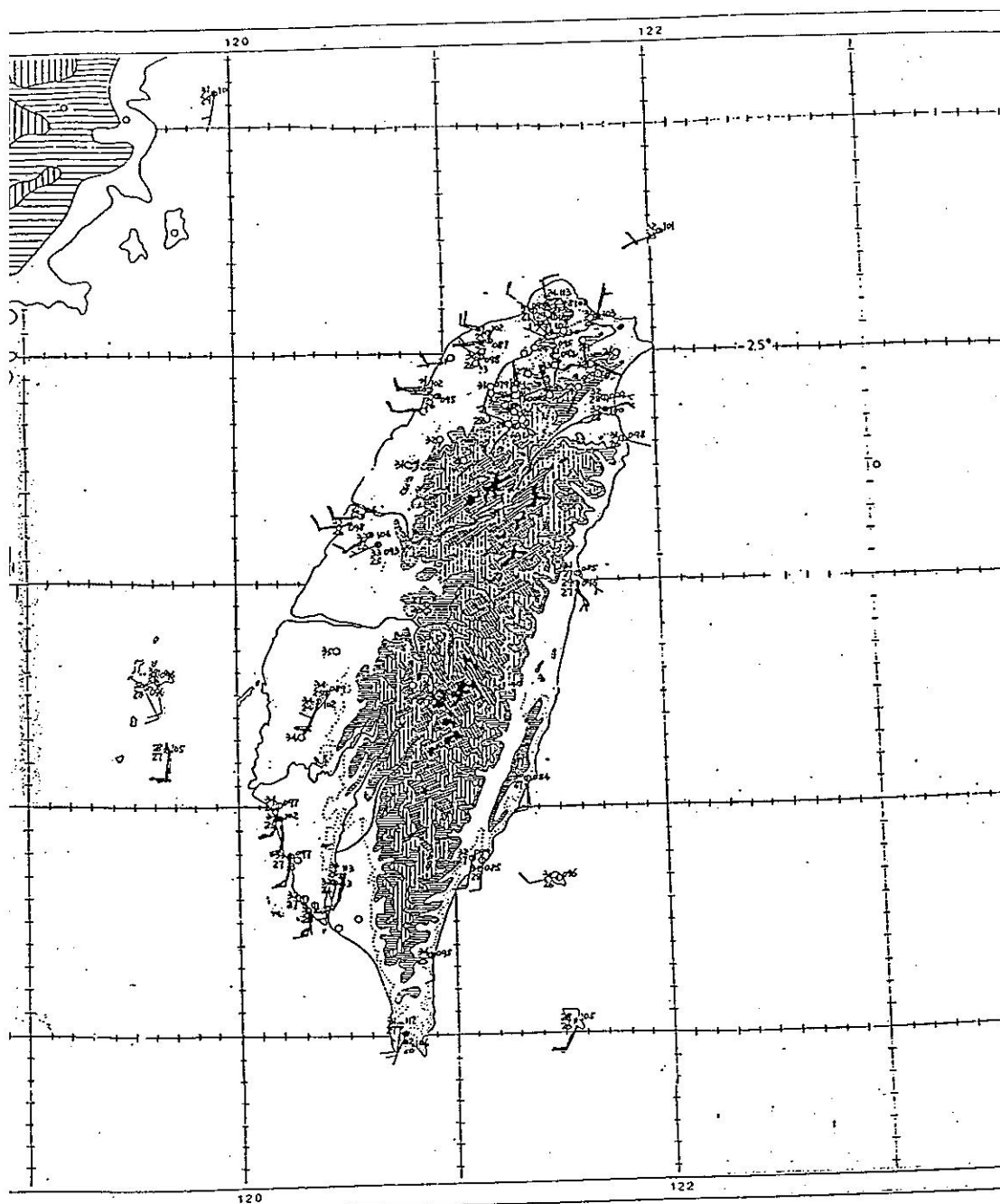
圖15a. 1987.6.20 1200 LST
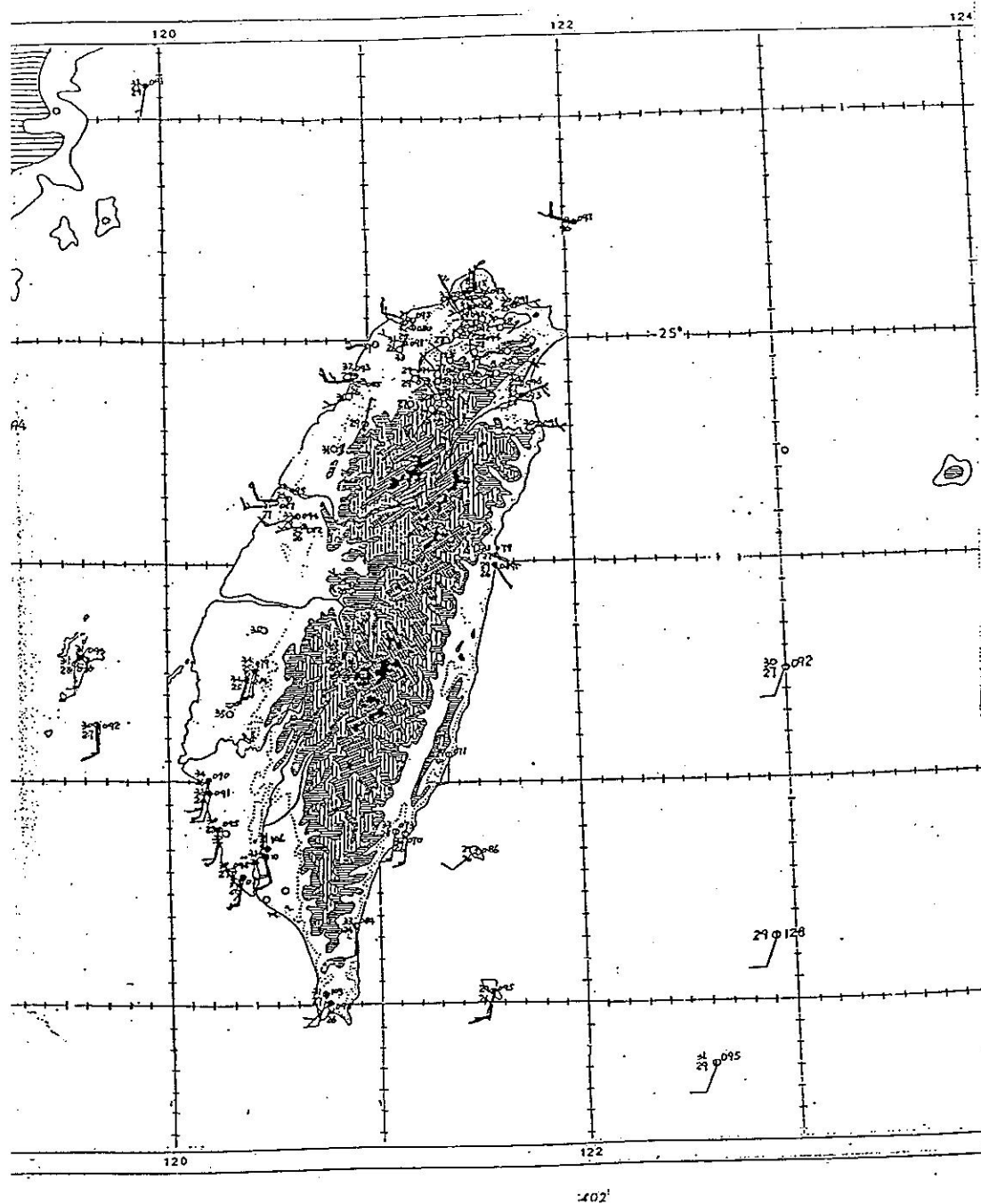
圖15b. 1987.6.20 1400 LST
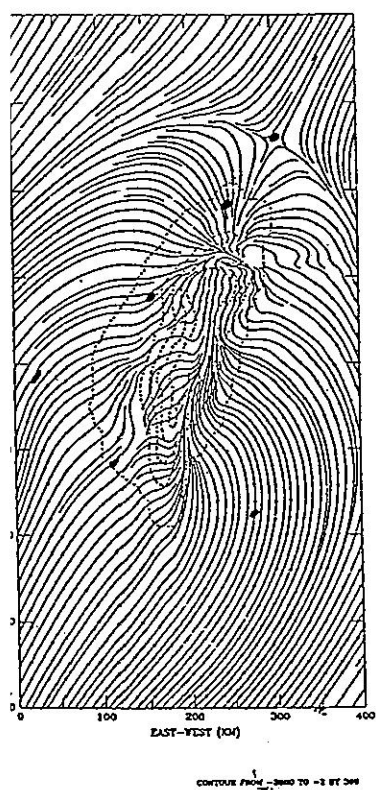
圖 16b. 模擬結果與圖 15b. 比較

圖 16a. 模擬結果與圖 15a. 比較

27
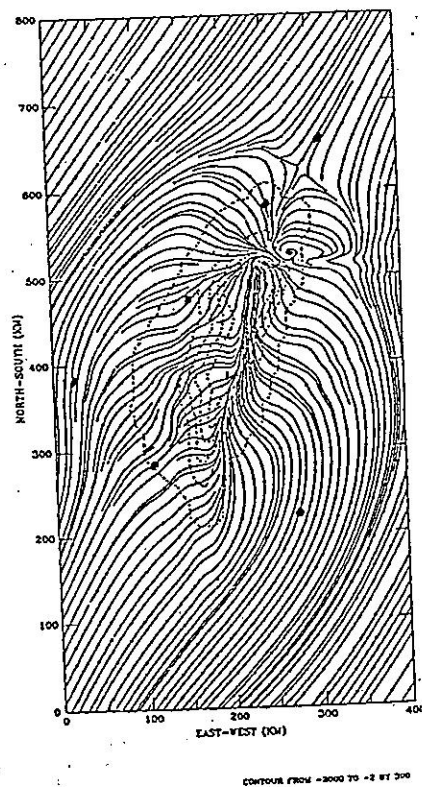
二、都普勒雷達資料分析

一資料特性：

　　自民國八十年秋季，中正機場都普勒雷達即可與中大大物所之電腦連線。這些資料是雷達掃描時之原始資料(rawdata)，以原來的體積掃描(Volume Scan)球面座標檔通過及電信局9600線路即時傳送，在中大的工作站可選擇性地顯示或存錄這些雷達資料。資料將包括回波強度(veflectivity)徑向風場(radial wind)及波譜寬(spectral width)，時間解析度可達每小時四次體積掃描。

二資料分析：

　　都普勒雷達資料在即時預報的應用可分成兩個階段的分析。

第一階段：資料偵錯及顯示
　　主要目的為PPI、RHI的顯示，但資料須經過初步的處理如
　　1去除地面回波
　　2去除雜訊

第二階段：診斷及研判
　　利用原始資料做進一步計算如
　　(1)VAD (Velocity azimuth display)　可分析平均風場輻散及變場
　　(2)VVP　　　　　　　　　　　　　可提供較粗解析度之二維風場
　　(3)TREC　　　　　　　　　　　　可提供回波移動速度
　　(4)wind shear estimation　　　　　可估計風切
　　(5)vertical velocity estimation　　　可估計垂直速度
　　(6)rainfall estimate　　　　　　　可估計雨量
　　(7)Interpolation　　　　　　　　可轉換成直角座標資料

三資料應用：

　　如資料分析軟體已完備時，即可開始針對不同的天氣發展即時預報之方法(algorithm)。如鋒面系統中鋒面位置、移速、風場、鋒面斜率、輻散場及變形場對鋒面結構之影響等。MCS中，中尺度渦旋、陣風鋒面偵測風場與深對流的關係等。

　　颱風系統：颱風中心位置眼牆上雨帶結構，環流與地形之關係等。　下面的圖為分析颱風個案的例子。
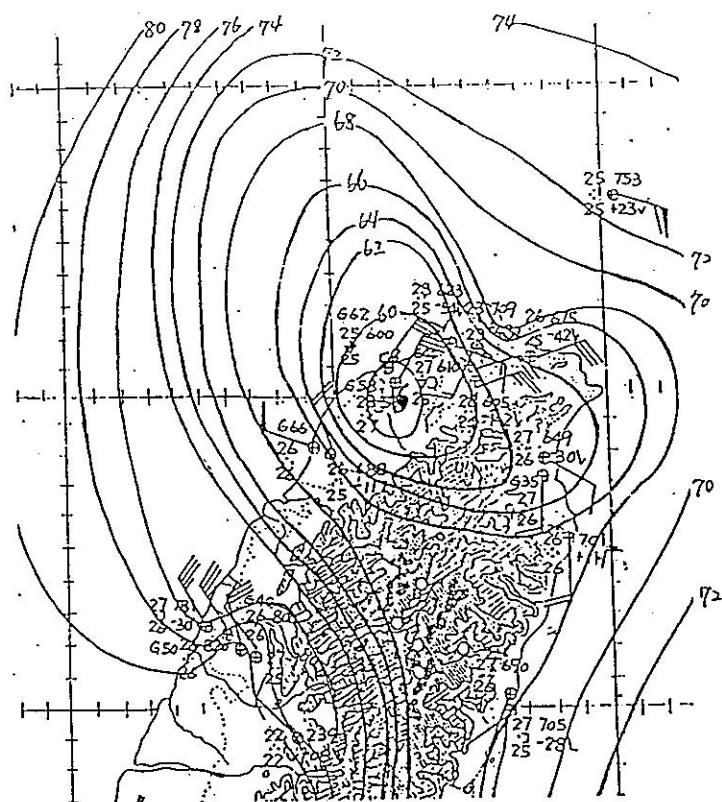
圖17. ：楊希颱風個案期間，8月19日1200LST地面填圖資料及氣壓分佈圖。
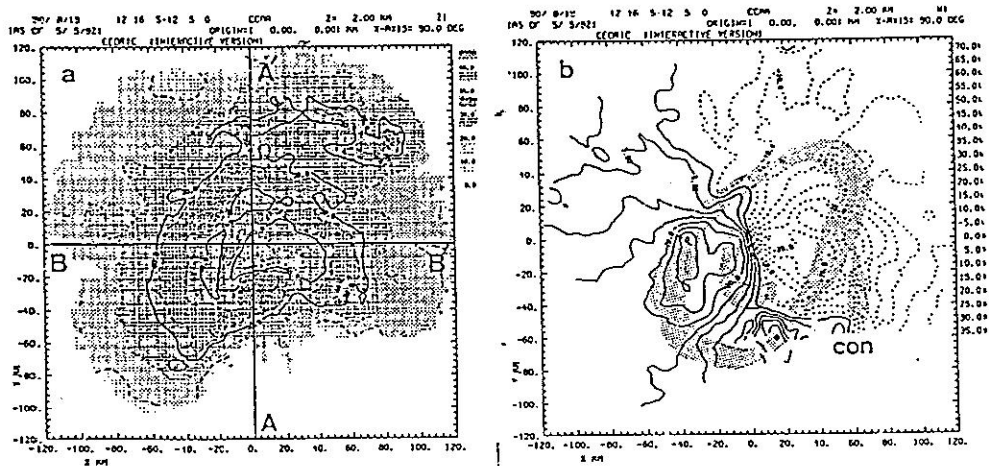
圖18.：a、b分別是8月19日1205LST中正雷達站觀測所得高度爲2公里
之雷達回波圖及徑向風場。
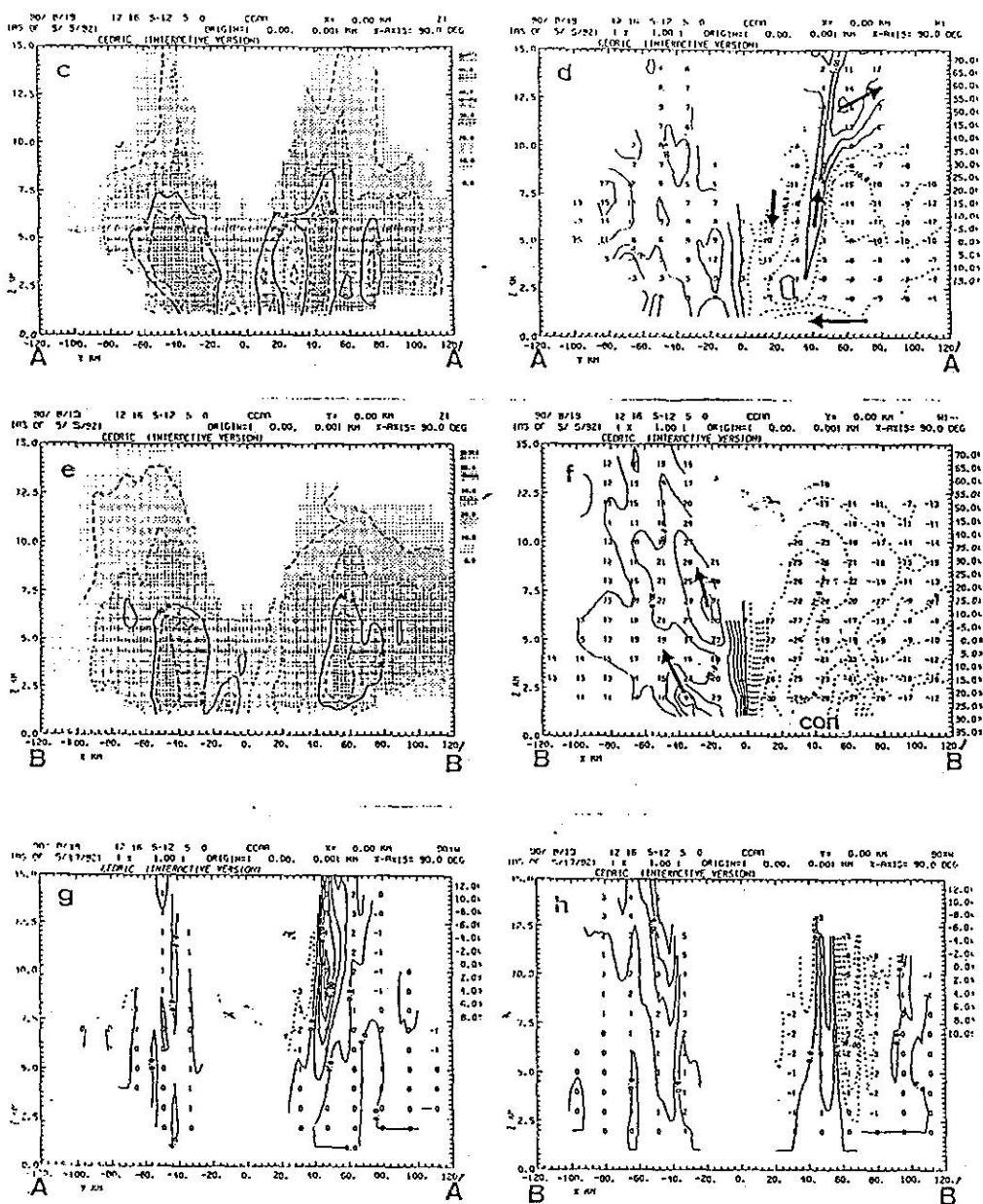
圖19.：c、d分別是圖a中AA'垂直剖面的雷達回波圖及徑向風場。e、
f分別是圖a中BB'垂直剖面的雷達回波圖及徑向風場。g、h分
別是圖a中AA'、BB'剖面的垂直速度估算結果。
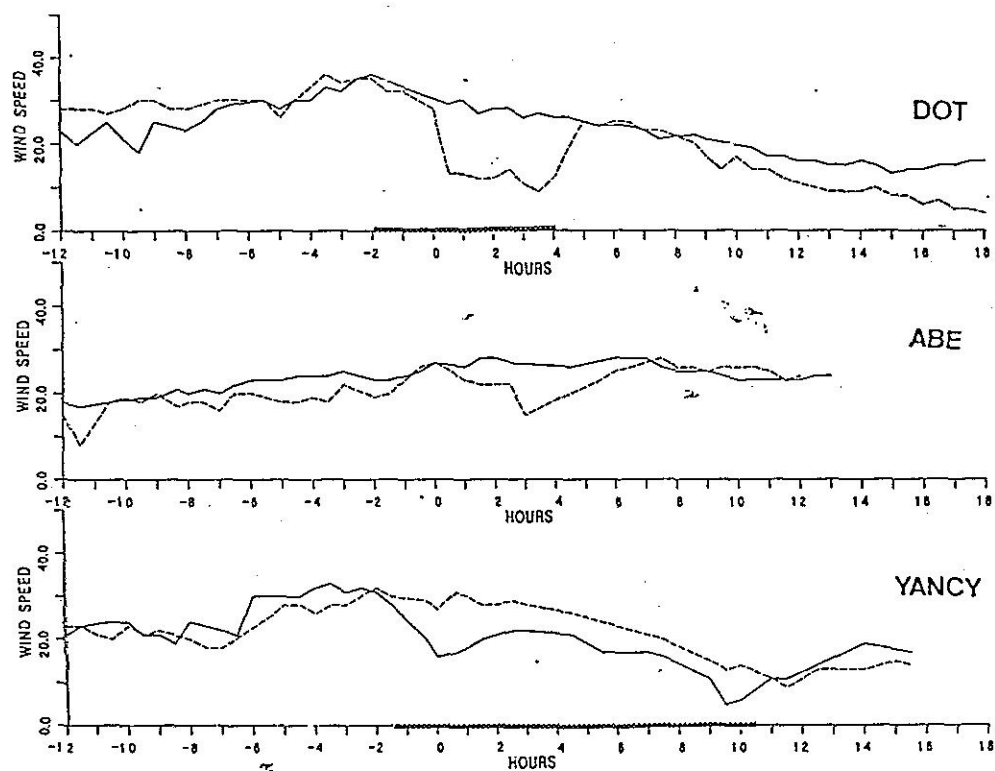
圖20: 中正都卜勒雷達所觀測之徑向風場以 VAD 技術分別估算三個颱
風(Yancy、Abe、Dot)登陸前後在雷達站附近之平均風場。
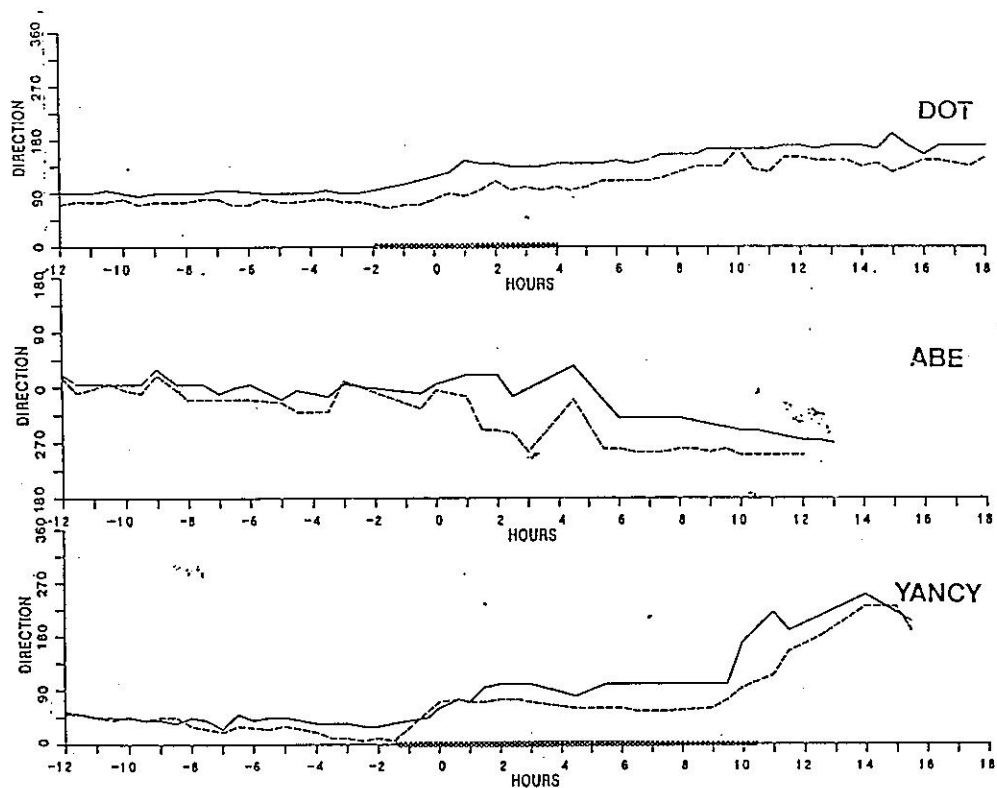
圖21.：中正都卜勒雷達所觀測之徑向風場以 VAD 技術分別估算三個颱
風(Yancy、Abe、Dot)登陸前後在雷達站附近之平均風向。
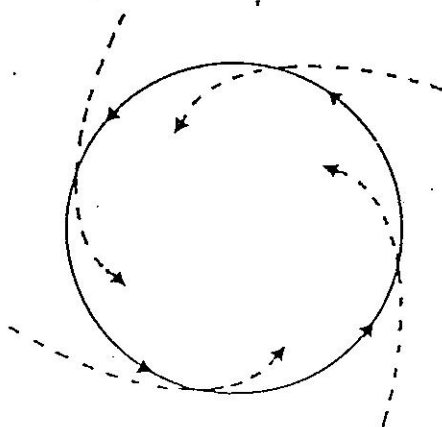
圖22 ：颱風環流中、低層風向之示意圖。
圖中虛線是低層氣流線方向
，而實線表中層流線方向。

32

　　台灣地區多山，降水系統常受到地形的影響在山區及斜坡上方發生，增長或消散。為了了解降水系統的特性，利用都普勒雷達資料來分析降水系統是可行的方法之一。目前分析方法大都假設地面邊界的垂直速度為零，這種假設在平地是很好的假設，但是在有地形時，由於地面的垂直速度是受到風速與地形斜率的影響，不一定為零，所以我們必須將目前分析方法加以修正。本報告提出的方法是將目前分析方法寫在地形座標上，因此地面的垂直速度自然隨著地面風速與地形斜率變化。如此，利用此修正方法所得的結果比較能分析山區降水系統低層的特性。詳細結果在附錄 A。

A Method to Obtain the Kinematic Structure of a Squall Line Derived from Dual-Doppler Radar in a Terrain-following Coordinate System

ZENSING DENG AND CHING-SEN CHEN

Institute of Atmospheric Physics
National Central University
Chung-Li, Taiwan, R.O.C.

34

A Method to Obtain the Kinematic Structure of a Squall Line Derived from Dual-Doppler Radar in a Terrain-following Coordinate System

ZENSING DENG AND CHING-SEN CHEN

Institute of Atmospheric Physics
National Central University
Chung-Li, Taiwan, R.O.C.

ABSTRACT

An alternative method to derive the wind field from dual-Doppler radar data in a mountainous area is given. This method is based on terrain-following coordinates in order to acquire more reasonable lower boundary conditions for the vertical velocity. First, we use dual-Doppler radar equations and the anelastic continuity equation as terrain-following coordinates to obtain the estimated wind direction and speed in three-dimensions. Then, we use the variational method to adjust the wind field by the constraint of the continuity equation.

After we compare the wind field obtained by this method (method A) with the model results and with that obtained by using a similar method in a cartesian coordinate system with a zero vertical velocity lower boundary condition (method B), we find that there is almost no difference between method A and B for flat terrain. However, fine structure associated with the terrain is found in method A. Ascending and descending motion occur to the wind-ward side and the lee side, respectively.

Key Words: kinematic structure, squall line, terrain-following coordinates

I. Introduction

The mountain ranges go north-south and are very lofty on the island of Taiwan. Mountains can have thermal and mechanical effects on the formation of precipitation system. So, many precipitation systems occur near or over mountainous areas. One of the methods used to study these systems is the analysis of Doppler data. In the past, many researchers have successfully achieved an understanding of the kinematic structure of precipitation systems via Doppler radar data. For example, Lin *et al.* (1990 a, b) and Mohr and Miller (1983) all used Doppler radar data to determine the kinematic structure of precipitation systems with the aid of SLU (Saint Louis University) and the CEDRIC (Custom Editing and Display of Reduced Information in Cartesian Space) package, respectively. The SLU package is the Doppler radar data analysis system developed at St. Louis University. (For details, see studies by Lin *et al.*, 1986) The CEDRIC package is the NCAR's (National Center of Atmospheric Research) Doppler radar analysis system (Mohr and Miller, 1983).

Lin *et al.* (1990a) discussed the kinematic structure of a squall line over the Taiwan Straits during TAMEX (Taiwan Area Mesoscale EXperiment) on May 16, 1987 by

using dual-Doppler radar data. Many important aspects of this system were revealed, such as a front-to-rear flow at all levels on the forward side of the squall line; a shallow rear-to-front flow at the back of the line; many individual cells imbedded within the squall line; new convective cells forming ahead of old cells; and convective downdrafts to the rear of the main updrafts.

The method used by Lin *et al.* as well as others to process the dual-Doppler radar data was constructed using a cartesian coordinate system. However, when we applied a similar method in Taiwan, we ran into some problems, for example, when we wanted to calculated the vertical velocity from the continuity equation in mountainous areas. The lower boundary condition was not necessarily zero, as assumed in the cartesian coordinate system. To overcome this problem, we have to use different coordinates for a better lower boundary to obtain the vertical velocity derived from Doppler radar data.

In this paper, we will derive a method which deals with Doppler radar data for a terrain-following coordinate system. Thus, the lower boundary condition can be easily determined from the wind speed and terrain features. We will then compare the internal kinematic structure of a convective system in northern Taiwan during TAMEX from our method with that derived from a method based on a

35

cartesian coordinate system.

II. Methodology

1. The Synthetic Method in Dual-Doppler Radar

To study the kinematic structure of a precipitation system, we need to know the horizontal (U, V) and vertical (W) velocity inside the precipitation system. If the Doppler radial velocity measured by two radars is represented by V_{r1} and V_{r2}, then the relationship between V_{r1} and V_{r2} and U, V and W can be written as

$$V_{r1} = U \sin\beta_1 \cos\theta_1 + V \cos\beta_1 \cos\theta_1 + W \sin\theta_1 \quad (1a)$$

$$V_{r2} = U \sin\beta_2 \cos\theta_2 + V \cos\beta_2 \cos\theta_2 + W \sin\theta_2, \quad (1b)$$

where β_1 and β_2 are the azimuth angle for the two radars, respectively. θ_1 and θ_2 are the elevation angle for the two radars, respectively and U, V and W are the particle moving speed components for the cartesian coordinate (as shown in Fig. 1).

For dual-Doppler radar conditions, the horizontal wind speed (U, V) can be solved with an unknown vertical wind speed (W_{air}):

$$U = U' + M_2 W_{air} \quad (2)$$
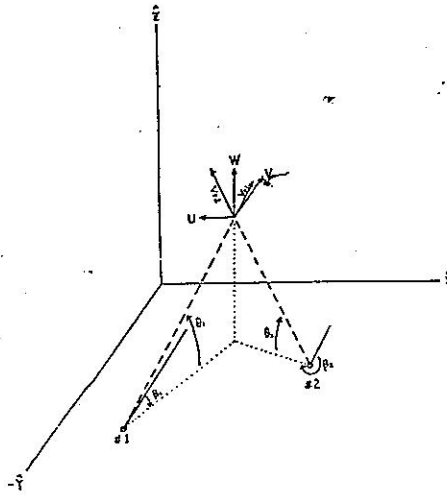
Fig. 1. Schematic depiction of dual-Doppler radar scanning of precipitation system particles. β_1 and β_2 are the azimuth angles, and θ_1 and θ_2 are the elevation angles for the two radars, respectively. U, V and W are the particle moving speed components in cartesian coordinates. V_{r1} and V_{r2} are the radial velocities for the two radars, respectively.

$$V = V' + M_4 W_{air} \quad (3)$$

where

$$U' = M_1 + M_2 V_t$$

$$V' = M_3 + M_4 V_t$$

$$M_1 = \frac{V_{r1} B_2 + V_{r2} B_1}{D}$$

$$M_2 = \frac{B_1 C_2 - B_2 C_1}{D}$$

$$M_3 = \frac{V_{r2} A_1 + V_{r1} A_2}{D}$$

$$M_4 = \frac{A_2 C_1 - A_1 C_2}{D}$$

$$A_i = \frac{x - x_i}{R_i}$$

$$B_i = \frac{y - y_i}{R_i}$$

$$C_i = \frac{z - z_i}{R_i}$$

$$D = B_2 A_1 - B_1 A_2$$

$$W = W_{air} + V_t$$

$$R_i = [(x - x_i)^2 + (y - y_i)^2 + (z - z_i)^2]^{\frac{1}{2}},$$

where (x_i, y_i, z_i) is the position of the ith radar. V_t is the terminal velocity of the precipitation particle and can be estimated by an empirical equation:

$$V_t = -4.32 \ (dBZ)^{0.0714286} \quad (4)$$

In Eqs. (2) and (3), there are three unknown variables (U, V, W_{air}), so we should add another equation using these three variables (usually, the continuity equation) if we want to solve them. The anelastic continuity equation for the terrain-following coordinate is

$$\frac{\partial \rho \dot\eta}{\partial \eta} = -(\frac{\partial \rho U}{\partial x} + \frac{\partial \rho V}{\partial x}) + S\rho U + P\rho V, \quad (5)$$

where

$$\eta = \frac{Z - Z_g}{Z_t - Z_g}$$

36

$$\dot{\eta} = \frac{d\eta}{dt}$$

$$S = \frac{1-\eta}{Z_t - Z_g} \frac{\partial Z_g}{\partial x}$$

$$P = \frac{1-\eta}{Z_t - Z_g} \frac{\partial Z_g}{\partial y}.$$

Z_g is the terrain height, Z_t is the model top height and ρ is the density of the air (as a function of height only). $\dot{\eta}$ is the vertical velocity of the terrain-following coordinate. From Eqs. (2), (3), and (5), we can derive a vertical difference equation for $\dot{\eta}$:

$$(\rho\dot{\eta})_c = (\rho\dot{\eta})_p - \delta\eta(\overline{\frac{\partial \rho U'}{\partial x} + \frac{\partial \rho V'}{\partial y}})_{p-c}$$

$$\text{A} \qquad \text{B} \qquad\qquad \text{C}$$

$$+ \delta\eta(\overline{S\rho U' + P\rho V'})_{p-c} - \delta\eta(\overline{\frac{\partial \rho M_2 W_{air}}{\partial x} + \frac{\partial \rho M_4 W_{air}}{\partial y}})_{p-c}$$

$$\text{D} \qquad\qquad\qquad \text{E}$$

$$+ \delta\eta(\overline{S\rho M_2 W_{air} + P\rho M_4 W_{air}})_{p-c}, \qquad (6)$$

$$\text{F}$$

where $()_c$ denotes the current layer data, $()_p$ denotes the previous layer (the upper layer in the downward integration) data, and $\overline{()_{p-c}}$ denotes the mean value of the two layers. The E and F terms can be divided into two parts:

$$E = E1 + E2 = -\frac{\delta\eta}{2}(\frac{\partial \rho M_2 W_{air}}{\partial x} + \frac{\partial \rho M_4 W_{air}}{\partial y})_p$$

$$-\frac{\delta\eta}{2}(\frac{\partial \rho M_2 W_{air}}{\partial x} + \frac{\partial \rho M_4 W_{air}}{\partial y})_c$$

$$F = F1 + F2 = \frac{\delta\eta}{2}(S\rho M_2 W_{air} + P\rho M_4 W_{air})_p$$

$$+ \frac{\delta\eta}{2}(S\rho M_2 W_{air} + P\rho M_4 W_{air})_c$$

Then, Eq. (6) can be represented as

$$A = B + C + D + E1 + E2 + F1 + F2 \qquad (7)$$

In the above equation, the B, C, D, E1 and F1 terms are known, but the A, E2 and F2 terms are unknown. To solve Eq. (8), we use the iterative method. The rewritten Eq. (7) for the mth iteration is

$$A_m = B + C + D + E1 + E2_{m-1} + F1 + F2_{m-1}, \qquad (8)$$

where W_{air}, used in $E2$ and $F2$, comes from the previous iteration. We continue the iteration involving the previous (p) and the current (c) levels until

$$|(\rho W_{air})_{c,m} - (\rho W_{air})_{c,m-1}| \le \varepsilon_0,$$

where $\varepsilon_0 = 0.001 \ kg/m^2 s$ in our calculation.

In Eq. (7), the unknown variables are $(W_{air})_c$ and $(\dot{\eta})_c$. The relationship between $(W_{air})_c$ and $(\dot{\eta})_c$ can be derived from coordinate transformation and Eqs. (2) and (3):

$$\rho W_{air} = (Z_t - Z_g)(\rho\dot{\eta} + \rho U'S + \rho V'P)/G, \qquad (9)$$

where

$$G = 1 - (Z_t - Z_g)[M_2 S + M_4 P].$$

Then, we can obtain the vertical wind speed (W_{air}) for every level by downward integration in Eq. (7). After W_{air} is obtained, U and V can be derived from Eqs. (2) and (3).

2. The Wind Adjusted by a Variational Method

In the above method, when we integrate the continuity equation, the error due to the finite difference accumulates in each vertical column. So, the 3-D wind field (U, V, W_{air}) derived from the above method is not consistent with the continuity equation. For this reason, we have to use a variational method to adjust the wind field, thus assuring that the continuity equation will be valid.

We use Eq. (5) as the constraint in the variational method. In Eq. (5), let $\rho\dot{\eta} = \hat{\dot{\eta}}$, $\rho U = \hat{U}$, $\rho V = \hat{V}$ and the hat is dropped:

$$\frac{\partial \dot{\eta}}{\partial \eta} = -(\frac{\partial U}{\partial x} + \frac{\partial V}{\partial x}) + SU + PV. \qquad (10)$$

Then the function of this variation using Eq. (10) as the constraint is

$$J = \iint \{\int [(U - \bar{U})^2 + (V - \bar{V})^2] d\eta$$

$$+ 2\lambda \int [(\frac{\partial U}{\partial x} + \frac{\partial V}{\partial y}) - SU - PV] d\eta\} dxdy, \qquad (11)$$

where $\bar{U}$ and $\bar{V}$ are the horizontal winds (multiplied by

the air density) derived from the above section. λ is the Lagrangian multiple.

In order to let $\delta J=0$ to minimize the function, we get

$$\iint \left\{ \int [(U-\bar{U})\delta U+(V-\bar{V})\delta V]d\eta \right.$$

$$+\left\{ \int [(\frac{\partial U}{\partial x}+\frac{\partial V}{\partial y})-SU-PV]d\eta \right\}\delta\lambda$$

$$+\lambda \left. \int [(\frac{\partial \delta U}{\partial x}+\frac{\partial \delta V}{\partial y})-S\delta U-P\delta V]d\eta \right\}dxdy=0. \tag{12}$$

From Eq. (12), we obtained the Euler-Lagrange equation,

$$U=\bar{U}+\frac{\partial\lambda}{\partial x}+S\lambda \tag{13}$$

$$V=\bar{V}+\frac{\partial\lambda}{\partial y}+P\lambda \tag{14}$$

$$\int_1^0 (\frac{\partial U}{\partial x}+\frac{\partial V}{\partial y}-SU-PV)d\eta=0, \tag{15}$$

and the natural boundary conditions. ($\lambda=0$ at the boundary; to be accurate, a discrete method should be used to derive Eqs. (13), (14) and (15).)

Deleting U and V by using Eqs. (13), (14) and (15), we obtain the equation λ

$$\int_1^0 [\frac{\partial^2\lambda}{\partial x^2}+\frac{\partial^2\lambda}{\partial y^2}+\frac{\partial}{\partial x}(S\lambda)+\frac{\partial}{\partial y}(P\lambda)-S\frac{\partial\lambda}{\partial x}-P\frac{\partial\lambda}{\partial y}$$

$$-\lambda(S^2+P^2)]d\eta=-\int_1^0 [\frac{\partial\bar{U}}{\partial x}+\frac{\partial\bar{V}}{\partial y}-S\bar{U}-P\bar{V}]d\eta. \tag{16}$$

Using the relaxation method to resolve $\lambda(x, y)$ from Eq. (16) and the natural boundary condition, we derive the horizontal wind field, which satisfies the continuity equation from Eqs. (13) and (14).

For the adjustment of the vertical velocity, we used Eqs. (13), (14), and (15) to delete the λ term as

$$\int_1^0 [\frac{\partial U}{\partial x}-\frac{\partial\bar{U}}{\partial x}+\frac{\partial V}{\partial y}-\frac{\partial\bar{V}}{\partial y}-S(U-\bar{U})-P(V-\bar{V})]d\eta$$

$$=-\int_1^0 [\frac{\partial\bar{U}}{\partial x}+\frac{\partial\bar{V}}{\partial y}-S\bar{U}-P\bar{V}]d\eta. \tag{17}$$

Let

$$D=\frac{\partial U}{\partial x}+\frac{\partial V}{\partial y}-SU-PV$$

$$D_0=\frac{\partial\bar{U}}{\partial x}+\frac{\partial\bar{V}}{\partial y}-S\bar{U}-P\bar{V}.$$

Then Eq. (17) can be written as

$$\int_1^0 (D-D_0)d\eta=-\int_1^0 D_0 d\eta=\dot{\eta}_0\Big|_{\eta=1},$$

where we use the top boundary condition ($\dot{\eta}_0|_{\eta=0}=0$). We obtain

$$\dot{\eta}_l-\dot{\eta}_{0l}=-\eta\dot{\eta}_0\Big|_{\eta=1}. \tag{18}$$

From Eq. (17), we know that the adjustment of $\dot{\eta}$ is proportional to η. Then, we can derive the vertical velocity (W_{air}) by using

$$\rho W_{air}=(Z_t-Z_g)[\rho\dot{\eta}+\rho U(1-\eta)S+\rho V(1-\eta)P]. \tag{19}$$

With the above method, we obtain the terrain-following three-dimensional wind field from dual-Doppler radar data, which satisfies the continuity equation. If we do not consider the terrain effects (or if the terrain is very flat in the radar analysis region), then the synthetic method described in section II.1 is similar to that in the CEDRIC package. The wind adjusted by the variational method described in section II.2 is similar to the SLU package.

III. Comparison with Two-dimensional Numerical Model Results

In this section, we want to demonstrate that the scheme mentioned in section II can obtain reasonable horizontal and vertical velocities. We assume that the radial velocity of the radar from a known wind field is obtained through two-dimensional numerical model results. Then, by using the method described in section II (hereafter called "method A"), we obtain U_a and W_a from this radial velocity. Comparing U_a and W_a with the model results (U, W), we expect to verify that the velocities obtained in method A will be very close to U and W.

Here, we choose the wind and reflectivity data from Chen's (1991) model results (shown in Fig. 2) as the actual wind and reflectivity data. Then, we project this known wind field to the radar scan line (assuming a radar position at $x=-10$ km and $z=0$ km) to get the 2-D radial wind data. The model's structure is similar to that described in very great detail by Durran and Klemp (1982). It is a two-dimensional version of the Klemp-Wilhelmson cloud model (Klemp and Wilhelmson, 1978) with a terrain-following coordinate system introduced. In addition, a wave-absorbing layer is added to the top of the domain. The rainwater variable for the model is the same as that in the Klemp-Wilhelmson model. The grid size in the x direction is constant and is taken to be 1 km, where it is stretched along the vertical to allow for finer resolution in the lower atmosphere. The model domain is 270×18.2 km². There was assumed to be a sponge layer 11 km thick at the top of the model.

In this model, because the horizontal wind (U) and vertical wind (W) are not at the same point for the nested grid system, W is moved to the locations of U before projection. Then, using the method described in section II (assumed in the two-dimensional plan) to obtain the wind field (U_a and W_a), we compare this wind field to that in the model.

Figure 3 presents the standard deviations of horizontal and vertical wind between the model results and the results of method A. The number on the vertical axis (K) of this figure is the vertical grid number in the model. The standard deviation of the horizontal wind is about 0.13 ms^{-1} and does not vary along the vertical axis. The maximum standard deviation of the vertical wind is about 0.125 ms^{-1} at about a height of 4.5 km ($K=10$). Using the maximum standard deviations and maximum values for the wind as obtained from the model in order to estimate the error of method A, we find that the errors for the horizontal and vertical wind are about 1 and 8 percent.

Figure 4 shows that U and W from the numerical model results (thick solid line) and the results using method A (thin solid line) at $x=4$ km (over low terrain) and $x=24$ km (over relatively steep terrain) vary with height. At $x=4$ km, the vertical wind speed is relatively small since no convection occurs in that region. The results of method A are very close to the model results for both horizontal and vertical wind. At $x=24$ km, this section passes through the convective region on the higher terrain. The horizontal winds from the model and from method A are quite similar. The vertical wind patterns for these two are also similar, but the maximum value from method A is somewhat larger than that from the model. The difference between the maximum vertical wind can also be seen in other sections (not shown). The alteration of vertical wind speed before projection and the finite difference method used to solve the vertical velocity
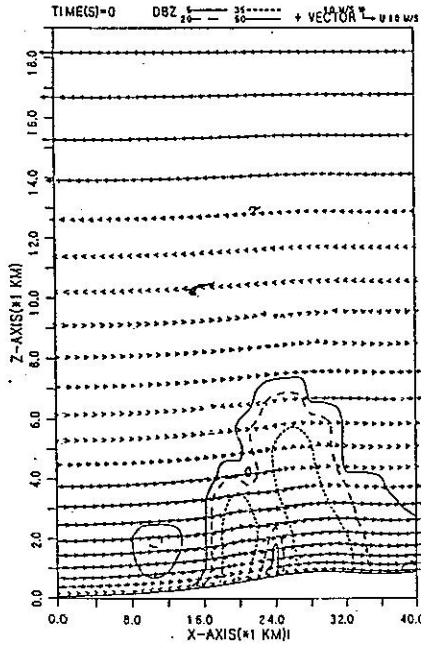

Fig. 2. The reflectivity pattern and wind field in a portion of the domain at a selected time from Chen's (Chen *et al.*, 1991) simulated results. The contour interval of the reflectivity is 15 dBZ, starting from 5 dBZ.
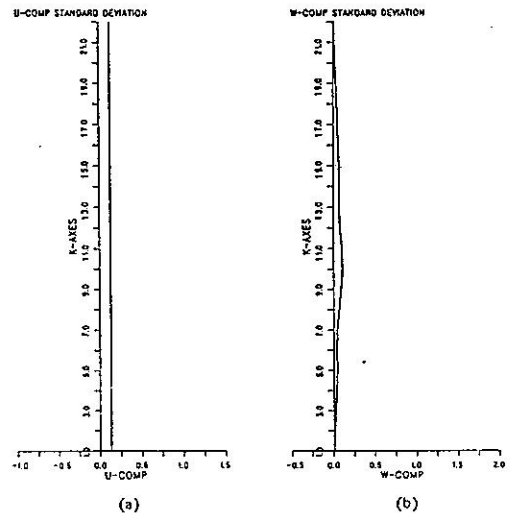

Fig. 3. The standard deviations of (a) horizontal and (b) vertical wind between the model results and the results obtained by using method A. The vertical axis is the vertical grid point number.
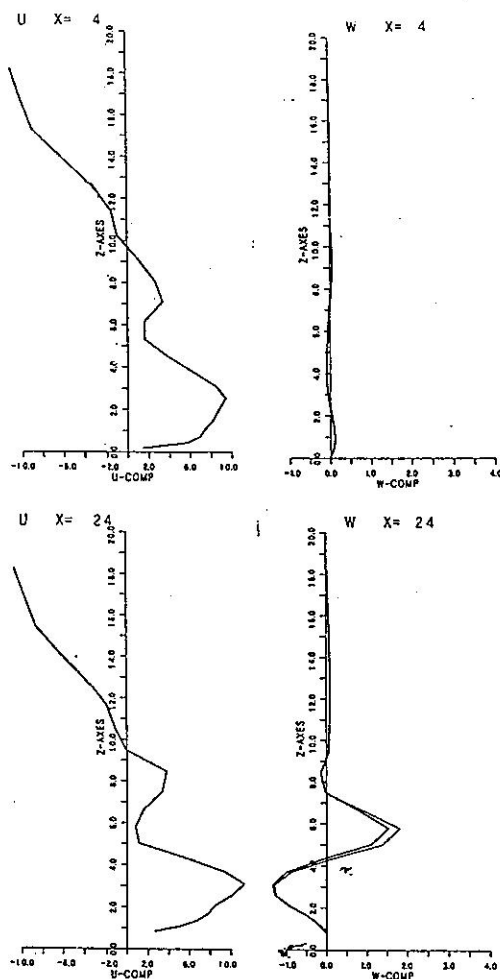
Fig. 4. The wind speeds of the model results (thick solid line) and results using method A (thin solid line) at x=4 km and x=24 km.

:may be the cause of this difference.

From the above discussion, the pattern or the value obtained using method A is reasonable, and we can say that method A is now available for research and operation work.

IV. Comparison to the Results Produced by CEDRIC Software with Cartesian Coordinates

We used method A to acquire the 3-D wind field for terrain-following coordinates and to find the kinematic structure of a precipitation system. We also interpolated the wind field to cartesian coordinates and used CEDRIC

software (hereafter to be called "method B") to find the kinematic structure of a precipitation system. Then, we compared the kinematic structures of both methods to see how they differed. We chose 01:30:00 on May 17, 1987 during TAMEX, when a squall line was moving toward a mountainous area. At this time, the convective region of the squall line was over relatively flat terrain. We compared the results produced by these two methods in this region to examine the reliability of method A. Moreover, we also compared the results of these two methods in mountain areas to see if there was any difference between them.

Three aspects are matched up here. First of all, horizontal sections from method A and method B are compared in order to search for a more generalized description, as well as to examine the differences and the similarities between the wind field analyzed by the two methods. Secondly, a comparison of south to north vertical sections is made to find the differences between the wind fields acquired in the squall line's convective region and in the mountain regions. Thirdly, a comparison of an east-to-west vertical sections produced by the two methods and applied to the two-dimensional wind field structure of the squall line's convective region is made to find differences in convection over mountain areas.

We hope that through the comparisons in this section, we will be able to determine why it would be better to use method A to process radar data in mountain areas.

All the coordinate systems used in analyzing radar data were fastened to the CP4 radar position, where the height was 9 meters at its horizontal origin.

1. Horizontal View

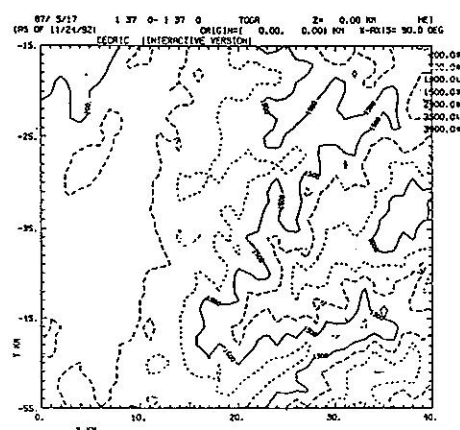Figure 5 shows the terrain in the radar data analysis

Fig. 5. Terrain chart of the radar analysis area. The contour interval is 500 m, starting from 500 m in height.

40

area. The altitude of the eastern side is higher. The altitude of 1000 m is found roughly to be at about x=20 km. Furthermore, it is obvious that there is a mountain ridge orientated in a northeast to southwest direction. There are two valleys oriented in the same direction located on either side of the mountain ridge, the highest peak of which has an altitude of 3400 m located at about x=38 km, y= -33 km.

A. z=3 km

Figures 6(a) and (b) indicate the horizontal wind superimposed with radar reflectivity and vertical velocity, as obtained by method A at z=3 km. Figure 7 is identical to Fig. 6 except that the results are obtained using method B. At this time, the convective region (with a reflectivity greater than 30 dBZ) of the squall line was located at approximately x=5 km. From Fig. 5, we know that the convective region was located in a flat area. There was little difference in the find field for x<15 km throughout the flat area. The main convergent area was located in the convective area or the front edge. The positions of the main ascending and descending regions are almost identical in the convective region and its neighboring area, but their values differed somewhat, mainly due to the difference in the smoothness technique used during data processing. There was more smoothing in method B. In the mountainous area (x>15 km), the vertical velocity was
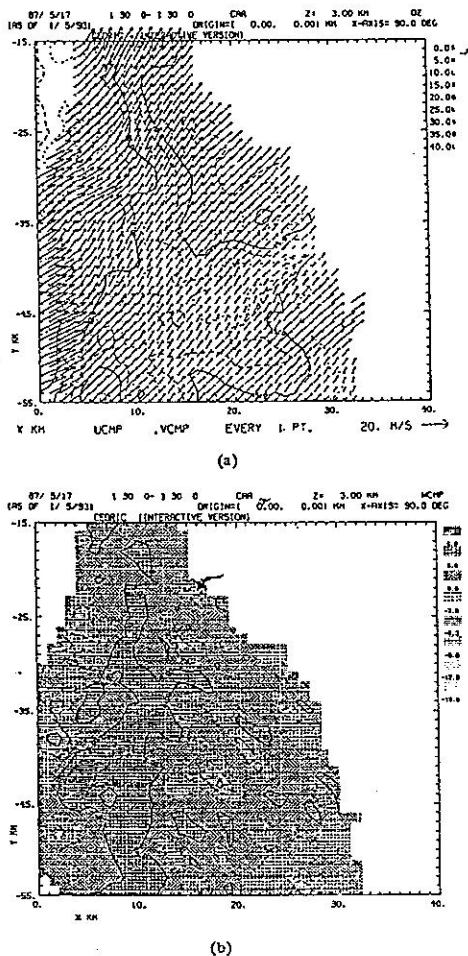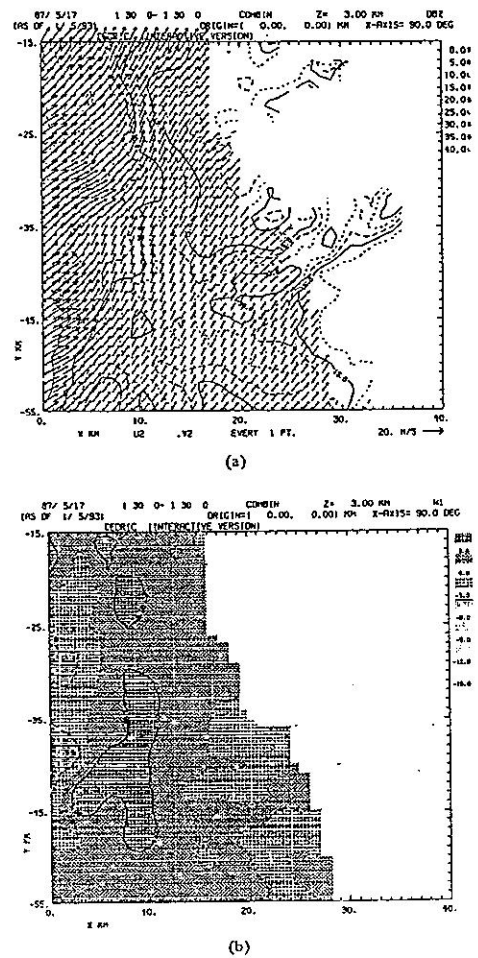

(a)

(b)

Fig. 6. The (a) horizontal wind and radar reflectivity and (b) vertical wind obtained by using method A at z=3 km. The contour interval of the reflectivity is 5 dBZ, starting from 0 dBZ. The contour interval of the vertical wind is $3ms^{-1}$, starting from $-15ms^{-1}$.

(a)

(b)

Fig. 7. Same as in Fig. 6, but for method B.

41

obviously different. Method A had more fine structures. For example, there were many upward and downward centers $x>15$ km, and $y>-45$ km, but in method B, downward motion dominated. These results were mainly produced by the different low boundary conditions used for the vertical velocity. In method A, the low boundary condition was $\dot{\eta}=0$, while the low boundary condition was $W=0$ for method B. Thus, in method A, upward or downward motion would occur when the air was moving up or down along the terrain. (This can be seen by comparing Fig. 6 with Fig. 5.)

B. z=5 km

At $z=5$ km (Figs. 8 (a), (b) and Figs. 9 (a), (b)), the difference between the horizontal wind was not very great except for some differences in results found in the upper
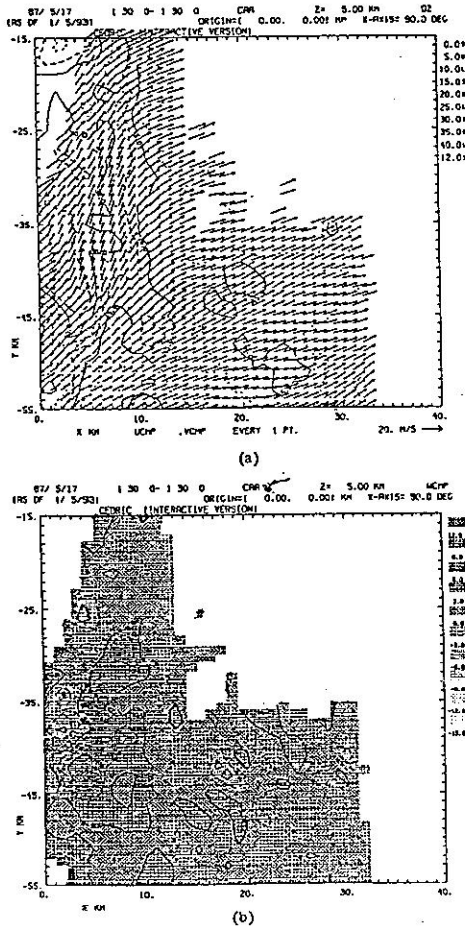

(a)

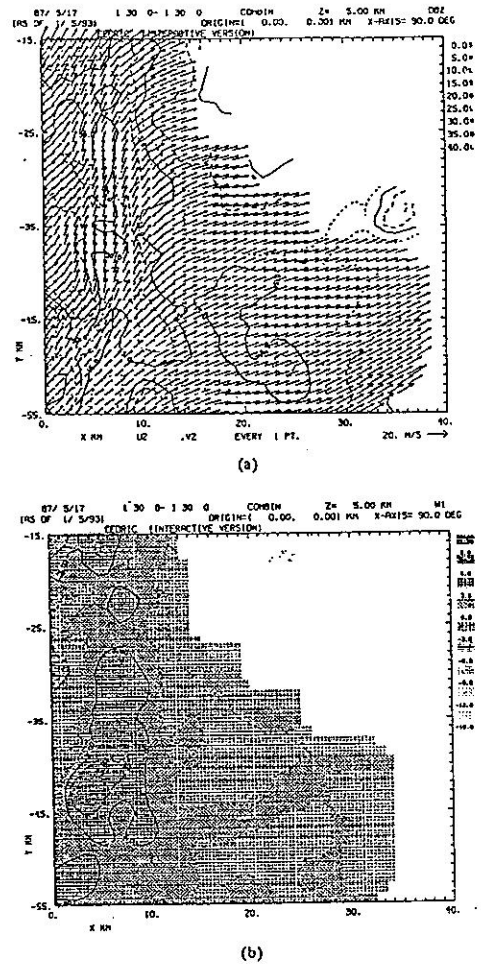(a)

(b)

Fig. 8. Same as in Fig. 6, but for z=5 km.

(b)

Fig. 9. Same as in Fig. 6, but for method B and z=5 km.

left area of the chart. This area was too close to the base line of the radars, therefore making the error in the synthetic process too large. Furthermore, there were still some other minor differences. For example, the wind pattern obtained by method B (Fig. 9 (a)) in the mountain area tended to be from the west rather than from the southwest as in method A (Fig. 8(a)). This was probably due to the lack of variational adjustment of the horizontal wind in method B. It may also have come from interpolation of the wind data from terrain-following coordinates to cartesian coordinates that was carried out in method A for the convenience of comparison.

The ascending and descending patterns in the convective region were identical. The maximum region was around ($x=4$ km, $y=-42$ km), but there were still some

differences in value. Moreover, in regions near the radar base line, there were obvious diversities because of poor calculation reliability. There were also obvious difference in mountain areas. For example, in one region of (16 km<x<25 km and -45 km<y<-35 km), there were two upward and two downward centers derived from method A (Fig. 8(b)), but no obvious upward motion in that region was obtained with method B (Fig. 9(b)).

2. South-to-North Vertical Section

Here, we want to compare the results derived from method A and B in two vertical sections at x=5 km and 20 km, respectively. The vertical section at x=5 km passed through the convective region of the squall line over a flat area. Another at x=20 km was over mountain areas.

A. x=5 km

Figure 10 (from method A) shows that there were four

areas having larger upward velocities (at y=-42 km, -35 km, -22 km and -18 km). Similarly, there were also 4 regions of higher upward velocity for method B (Fig. 11), and their positions were identical to those in method A. However, the magnitude of the second region's (y=-35 km) larger upward velocity was not so obvious as that in Fig. 10. The larger vertical velocity in this region derived from method A was caused by the low reliability of the horizontal wind close to the radar base line as seen in Fig. 8.

In addition, there were some differences at the low level in results obtained by using the two methods. For example, the downward motion bet than -35 km<y<-25 km derived from method A was bigger than that obtained from method B. In method B, the low boundary condition of the vertical velocity was zero. Although the terrain of this region was flatter, the wind velocity on the lower level was strong. Therefore, certain differences resulted.

B. x=20 km

This section cut through the mountain area. From Figs. 6 and 7, we see that on the lower level of this area,

(a)

(b)

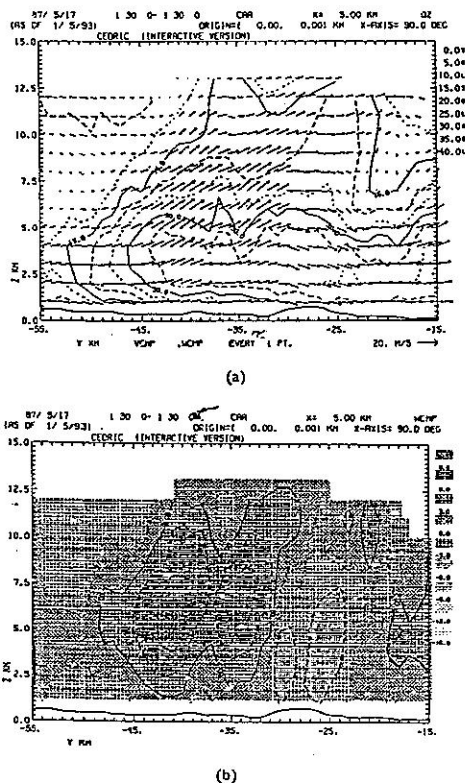Fig. 10. The (a) wind field and radar reflectivity and (b) vertical wind obtained by using method A at x=5 km. The contour interval of the reflectivity is 5 dBZ, starting from 0 dBZ. The contour interval of the vertical wind is 3ms⁻¹, starting from -15ms⁻¹.
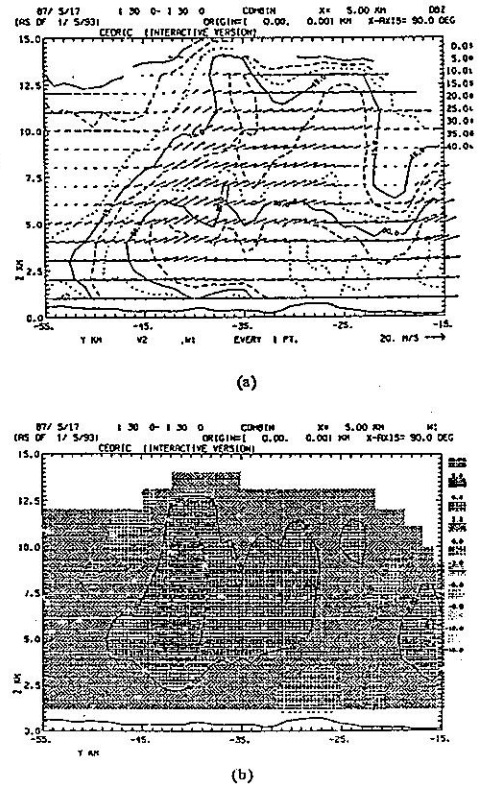

(a)

(b)

Fig. 11. Same as in Fig. 10, but for method B.

the wind blew northward. Therefore, from method A (Fig. 12), we see that the flow ascended and descended according to the rising and falling of the mountains. This phenomenon shows good agreement between the movement of flow and terrain features. In method B (Fig. 13), however, the airstream moved almost horizontally, and the vertical velocity was very small.

3. East-to-West Vertical Section

The east-to-west section is perpendicular to the squall line. The kinematic structure of this section could help us understand the structure of a squall line. We chose the vertical section located at $y=-44$ km from the radar base line.

In this section (Fig. 14 and Fig. 15), we could see that the main part of the squall line was located at $x=4$ km. In front of the squall line, at about $x=10$ km, there was a new cell. Both had their own ascending area. Except for some minor differences for $x<10$ km, the results of method A and B are similar. To the right of the new cell

(a)

(b)

Fig. 13. Same as in Fig. 10, but for method B and $x=20$ km.

around $x=20$ km, there was a cell which did not develop highly. Here the differences between the two methods were large. In method B (Fig. 15), the movement of the flow was mainly horizontal, and the vertical velocity was very small, yet in method A , it is obvious that the air ascended and descended closely following the topography.

V. Conclusion

An alternative method (method A) with terrain-following coordinates for dual-Doppler radar analysis has been used to overcome the zero vertical velocity of the lower boundary conditions for the existing method in more complex terrain. The method we derived was tested against numerical model results. We found that the difference of the velocity field between our method and the model results was small. When we analyzed the true radar data for TAMEX IOP #2 using either method A or the CEDRIC method (method B) in a cartesian coordinate system, the qualitative features of the convective region's velocity field for a squall line were similar
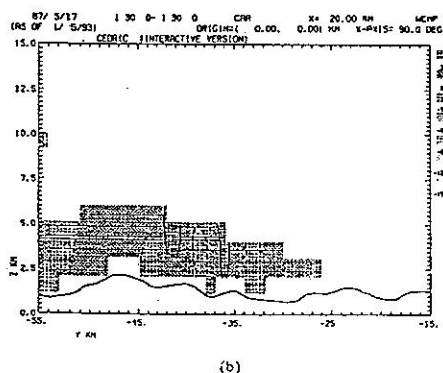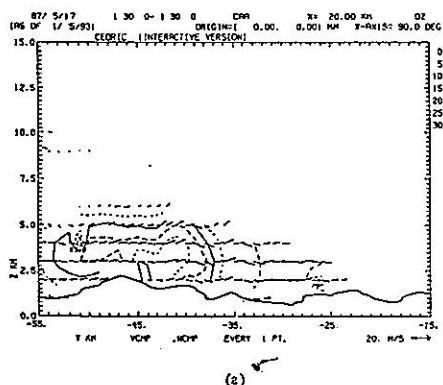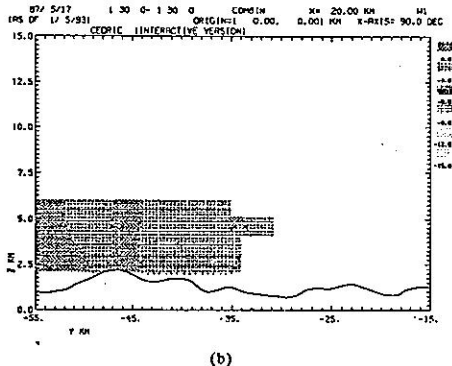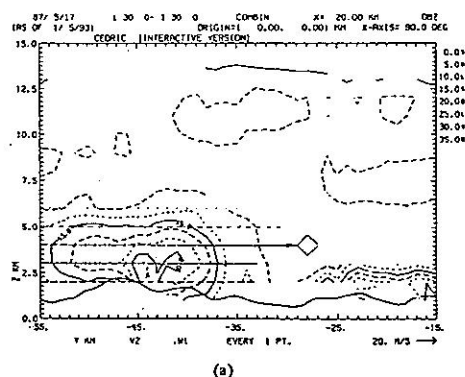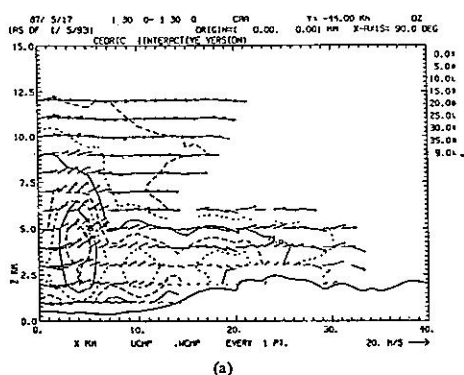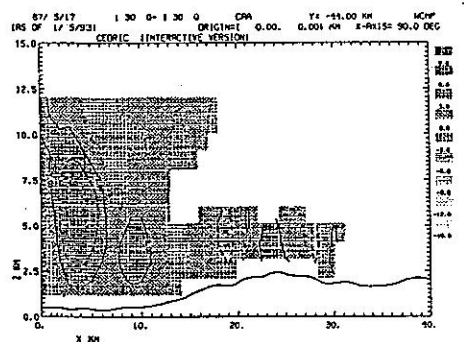
(a)

(b)

Fig. 12. Same as in Fig. 10, but for $x=20$ km.

44

(a)

(b)

Fig. 14. Same as in Fig. 10, but for y=-42 km.

(a)

(b)

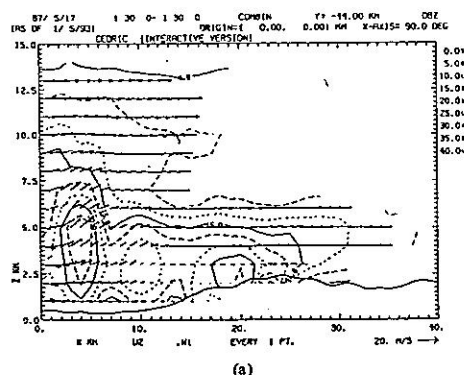Fig. 15. Same as in Fig. 10, but for method B and y=-42 km.

for flatter terrain, but there were some differences for velocity fields in mountain regions. Finer features associated with the terrain were found in method A. Ascending and descending motion occurred to the wind-ward side and the lee side, respectively.
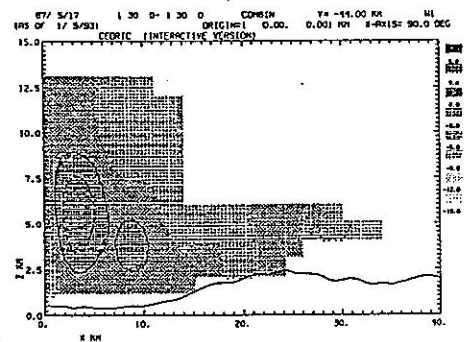
Acknowledgments

References

Chen, C.-S., W.-S. Chen, and Z.-S. Deng (1991) A study of a mountain-generated precipitation system in northern Taiwan during TAMEX IOP 8. *Mon. Wea. Rev.*, 119, 2574-2606.

Durran, D. R. and J. B. Klemp (1982) The effects of moisture on trapped mountain lee waves. *J. Atmos. Sci.*, 39, 2490-2506.

Klemp, J. B. and R. B. Wilhelmson (1978) The simulation of three-dimensional convective storm dynamics. *J. Atmos. Sci.*, 35, 1070-1096.

Lin, Y.-J., T. C. Wang, R. W. Pasken, and H. Shen (1990a) Characteristics of a substropical squall line determined from TAMEX dual-Doppler data. Part I: Kinematic structure. *J. Atmos. Sci.*, 47, 2357-1381.

Lin, Y.-J., T. C. Wang, R. W. Pasken, H. Shen, and Z.-S. Deng (1990b) Characteristics of a subtropical squall line determined from TAMEX dual-Doppler data. Part II: Dynamic and Thermodynamic structure and momentum budgets. *J. Atmos. Sci.*, 47, 2382-2399.

Lin, Y.-J., T. C. Wang, and J. H. Lin (1986) Pressure and temperature perturbations within a squall-line thunderstorm derived from SESAME dual-Doppler data. *J. Atmos. Sci.*, 43, 2302-2327.

Mohr, C. G. and L. J. Miller (1983) CEDRIC - A software package for cartesian space editing, synthesis and display of radar field under interactive control. 21st conference on Radar Meteorology, Boston, Amer. Meteor. Soc., 569-574.